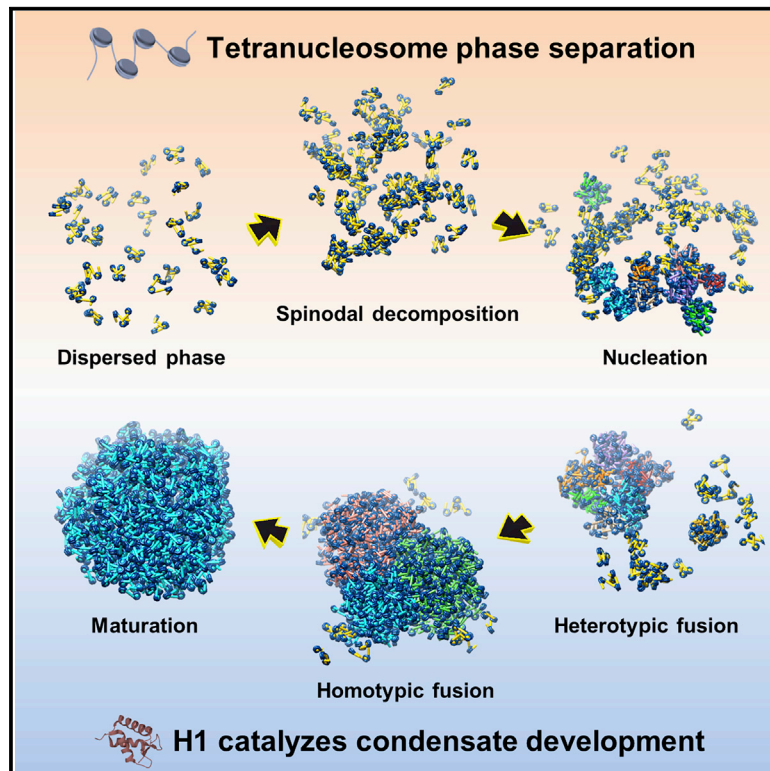Article

Molecular organization of the early stages of nucleosome phase separation visualized by cryo-electron tomography

Graphical abstract

Authors

Meng Zhang, César Díaz-Celis, Bibiana Onoa, ..., Eva Nogales, Gang Ren, Carlos Bustamante

Correspondence

gren@lbl.gov (G.R.), carlosjbustamante2@gmail.com (C.B.)

In brief

Zhang et al. demonstrate that liquid-liquid phase separation of tetranucleosome arrays occurs in two steps: a spinodal decomposition involving formation of loosely arranged irregular condensates, followed by the emergence of tightly packed spherical nuclei. The structure of nucleosome condensates by cryo-ET suggests a physical mechanism of chromatin compaction *in vivo*.

Highlights

- Tetranucleosome phase separation involves a two-step condensation process

- Spinodal decomposition causes the initial formation of loosely packed irregular condensates

- Nuclei formation within spinodal condensates gives raise to denser spherical condensates

- Histone H1 catalyzes more than 10-fold the spinodal-to-spherical condensate conversion

CellPress

Molecular Cell

Article

Molecular organization of the early stages of nucleosome phase separation visualized by cryo-electron tomography

Meng Zhang,[1,2,8,10] César Díaz-Celis,[2,3,10] Bibiana Onoa,[3] Cristhian Cañari-Chumpitaz,[4] Katherinne I. Requejo,[2,3] Jianfang Liu,[8] Michael Vien,[5] Eva Nogales,[2,3,6,7] Gang Ren,[8,*] and Carlos Bustamante[2,3,4,5,6,7,9,11,*]

[1]Applied Science and Technology Graduate Group, University of California, Berkeley, CA, USA
[2]California Institute for Quantitative Biosciences, University of California, Berkeley, CA, USA
[3]Howard Hughes Medical Institute, University of California, Berkeley, CA, USA
[4]Department of Chemistry, University of California, Berkeley, CA, USA
[5]Department of Physics, University of California, Berkeley, CA, USA
[6]Department of Molecular and Cell Biology, University of California, Berkeley, CA, USA
[7]Molecular Biophysics and Integrative Bioimaging Division, Lawrence Berkeley National Laboratory, Berkeley, CA, USA
[8]The Molecular Foundry, Lawrence Berkeley National Laboratory, Berkeley, CA, USA
[9]Kavli Energy Nanoscience Institute, University of California, Berkeley, CA, USA
[10]These authors contributed equally
[11]Lead contact
*Correspondence: gren@lbl.gov (G.R.), carlosjbustamante2@gmail.com (C.B.)
https://doi.org/10.1016/j.molcel.2022.06.032

SUMMARY

It has been proposed that the intrinsic property of nucleosome arrays to undergo liquid-liquid phase separation (LLPS) *in vitro* is responsible for chromatin domain organization *in vivo*. However, understanding nucleosomal LLPS has been hindered by the challenge to characterize the structure of the resulting heterogeneous condensates. We used cryo-electron tomography and deep-learning-based 3D reconstruction/segmentation to determine the molecular organization of condensates at various stages of LLPS. We show that nucleosomal LLPS involves a two-step process: a spinodal decomposition process yielding irregular condensates, followed by their unfavorable conversion into more compact, spherical nuclei that grow into larger spherical aggregates through accretion of spinodal materials or by fusion with other spherical condensates. Histone H1 catalyzes more than 10-fold the spinodal-to-spherical conversion. We propose that this transition involves exposure of nucleosome hydrophobic surfaces causing modified inter-nucleosome interactions. These results suggest a physical mechanism by which chromatin may transition from interphase to metaphase structures.

INTRODUCTION

The genome of eukaryotic cells is organized into chromatin, a protein-DNA complex whose structure regulates processes such as transcription and replication. The nucleosome is the basic structural unit of chromatin consisting of 146 bp of DNA wrapped 1.65 turns around a histone core (Luger et al., 1997). A set of modifications of histones and associated proteins modulate the structural dynamics of chromatin (Bowman and Poirier, 2015), which form two distinct nuclear subdomains: a lightly packed euchromatin state, associated with regions of active transcription and a condensed heterochromatin state, that represent transcriptionally repressed regions.

There are two models that attempt to explain how chromatin transitions between its transcriptionally active and inactive forms. One model identifies the euchromatin regions with the 10-nm fiber ("beads on a string"). This fiber is proposed to fold in a compact and helical structure displaying a 30 nm diameter (Finch and Klug, 1976; Robinson et al., 2006; Song et al., 2014; Widom and Klug, 1985) that comprises the heterochromatin domains. In this hierarchical folding model, chromatin condenses through various super-helical structural intermediates formed at different stages of the cell cycle (Belmont and Bruce, 1994). However, this model has been challenged due to the lack of evidence of the 30 nm fiber *in vivo* (Cai et al., 2018a; Eltsov et al., 2008, 2018; Maeshima et al., 2014a, 2014b; Nishino et al., 2012; Ou et al., 2017; Razin and Gavrilov, 2014).

An alternative model for chromatin organization has been proposed recently based on the intrinsic property of chromatin to form liquid-like droplets by liquid-liquid phase separation (LLPS), both *in vitro* and *in vivo* (Gibson et al., 2019; Maeshima et al., 2016; Sanulli et al., 2019; Strom et al., 2017). LLPS is a

physical process that generates spatially separated membrane-less domains inside the cell (Banani et al., 2017; Boeynaems et al., 2018; Brangwynne et al., 2009; Erdel and Rippe, 2018; Hubstenberger et al., 2017; Hyman et al., 2014; Sanulli and Narlikar, 2020); optically, they appear as liquid droplets that coexist with a dilute phase (Boeynaems et al., 2018).

In this recent LLPS model, the phase transition of chromatin into droplets drives compartmentalization and organization of long-lasting multiphase systems (Palikyras and Papantonis, 2019; Shakya et al., 2020), which has been posited to control chromatin accessibility by the cellular machinery (Palikyras and Papantonis, 2019; Shin et al., 2018; Wright et al., 2019). *In vitro*, fluorescence microscopy studies have revealed that nucleosome phase transition is regulated by nucleosome concentration, nucleosome array length, nucleosome dynamics, DNA linker spacing, ionic strength, and chromatin-associated proteins such as heterochromatin protein 1 (HP1) and linker histone H1 (Gibson et al., 2019; Maeshima et al., 2016; Sanulli et al., 2019; Zhang and Kutateladze, 2019). These studies are, however, circumscribed to late stages of the process when phase-separated condensates reach micron sizes. Thus, a number of questions remain unanswered: what is the physical process through which macroscopic domains arise from the nucleosome components? Do phase-separated condensates form through a classical mechanism of nucleation and growth? If chromatin condensates act as compartments to facilitate or prevent specific enzymatic reactions, they should be able to transition from loosely to tightly packed structures (Bancaud et al., 2009; Imai et al., 2017). What is then the condensates' internal nucleosomal organization to enable these dynamics? Is the nucleosome spatial distribution in the condensates homogeneous or do channels and/or chambers exist to facilitate molecular diffusion?

Addressing the above questions requires imaging nucleosomes inside the condensates; yet, given their heterogeneous nature, structural averaging methods such as X-ray crystallography or single-particle reconstruction are inadequate. Fortunately, improvement of cryo-electron tomography (cryo-ET) as a single-molecule 3D imaging technique (Chen et al., 2017; Ercius et al., 2015; Narayan and Subramaniam, 2015; Zhang and Ren, 2012) has made it possible to obtain 3D structures at molecular resolution (Jordan et al., 2018; Lei et al., 2018; Ou et al., 2017; Zhang et al., 2016). Here, we systematically study, *in vitro*, the initial stages of nucleosomal phase separation using reconstituted tetranucleosome arrays and cryo-ET reconstruction coupled to deep-learning-based denoising and segmentation protocols. Tetranucleosome arrays constitute the minimal unit capable of organizing large-scale chromatin structures and undergo phase separation (Ding et al., 2021; Schalch et al., 2005; Song et al., 2014).

We find that the initial stages of phase separation take place through a two-step condensation process. The first step resembles a spinodal decomposition in which a nucleosome-rich phase composed of irregularly shaped and loosely packed condensates emerges at physiological salt. In the second step, spherical nuclei (as small as ~35 nm) arise within the spinodal condensates (SpnCs); they appear to grow into larger spherical condensates (SphCs) through the accretion of nearby spinodal materials or through fusion with other SphCs. Their spherical shapes indicate that formation of these aggregates involves an initial unfavorable surface free energy that must be minimized relative to their favorable volume energy. Furthermore, the binding of H1 linker histones catalyzes the transition from SpnC to SphC more than 10-fold.

RESULTS

Observation of the early stages of condensation by cryo-ET

To study chromatin LLPS, we used *Xenopus laevis* recombinant tetranucleosomes assembled on a DNA fragment containing four 601-nucleosome positioning DNA sequences separated by 40 bp linkers (Figure 1A). Nucleosome phase-transition time course experiments started by diluting the tetranucleosomes arrays to 30 nM either in a low ionic strength buffer or in a physiological salt concentration buffer (see STAR Methods). We used optimized negative staining (OpNS) (Rames et al., 2014) and EM imaging to improve deposition conditions and to establish the time required for condensate formation.

At the earliest incubation/deposition time (2 min, at 20°C) in physiological salt buffer (150 mM NaCl and 5 mM MgCl$_2$), we observed nucleosome condensates of irregular shapes (Figures S1A and S1B). These condensates were absent at low salt buffer (1.5 mM NaCl, no MgCl$_2$; Figure S1C). Interestingly, after 10 min of incubation, small globular condensates (~35–40 nm in diameter) with higher nucleosomal density appeared sparsely among the irregularly shaped nucleosome structures (Figures S1A and S1D). The shape of these globular condensates was variable; some were rounded, while others were elongated and composed of a dense, rounded condensate connected with an irregular region (Figures S1D and S1E, white arrow).

After 30 min of incubation, larger SphCs (>100 nm diameter) emerged, which increased in number and size at longer incubation times (Figures S1A and S1B). Compared with the surrounding irregular condensates, the SphCs appear to be composed of tightly packed nucleosome core particles (NCPs) (Figure S1F). Statistical analysis of the SphC grid surface density showed that their rate of formation is temperature dependent (fast to slow: 20°C, 36°C, and 4°C; Figure S1B). Furthermore, epifluorescence microscopy of equivalent samples showed fusion events (Figure S2A), indicating that the condensates observed by OpNS behave like the liquid droplets previously described (Gibson et al., 2019). The liquid-like behavior of the condensates was further confirmed by fluorescence recovery after photobleaching (FRAP) experiments (Figure S2B). The diffusion of our tetranucleosome condensates (t$_{1/2}$ = 1 min) is faster than that reported for dodecameric condensates (t$_{1/2}$ = 6 min) (Gibson et al., 2019). To determine whether this two-step condensation process is a property of nucleosome arrays, independent of their length, we also performed analogous experiments but using dodecamer arrays (Figure S3A). Indeed, the dodecamer and tetramer results are in good agreement (Figure S3B), although the SphCs formation was ~10-fold faster with the longer arrays.

To capture the rapidly formed, irregular condensates at the earliest imaging time, we collected tomographic data of the phase-transition reaction of tetranucleosome arrays (25% harbored a biotin molecule at one DNA end) after 2 min but in low salt (15 mM Na$^+$), and then at 2 and 10 min in physiological
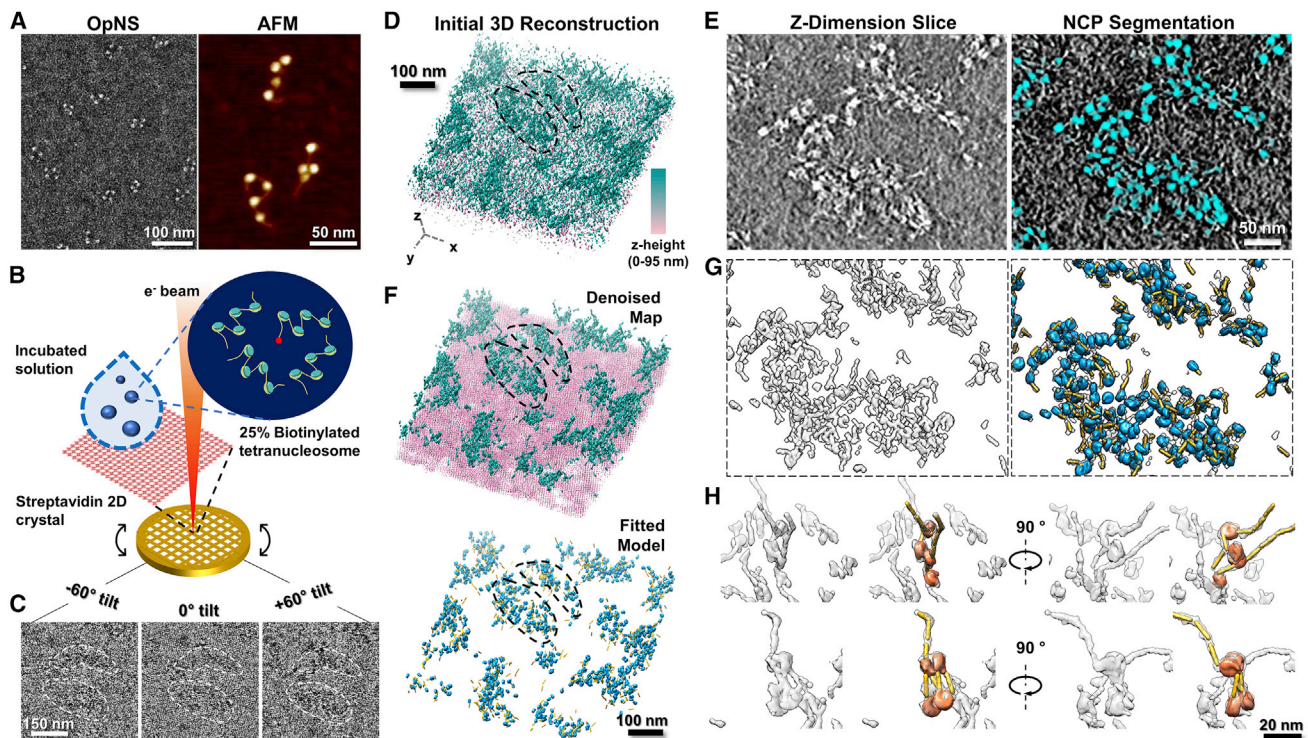
Molecular Cell
Article

Figure 1. Cryo-ET workflow of deposition, reconstruction, and modeling of tetranucleosome phase-separated condensates

(A) Optimized negative staining EM and AFM images of tetranucleosomes.

(B) Deposition of 30 nM (25% biotinylated; red sphere) tetranucleosome incubation solution onto the SA crystal.

(C) Representative tilt series after deep-learning-based denoising. White dashed contours depict two tracked clusters of condensates.

(D) Initial 3D reconstruction of denoised and aligned tilt series with z-dimensional height encoded in color.

(E) Central slice of the initial map (thickness of 7.02 nm, left) and corresponding deep-learning-based segmentation showing predicted NCPs (cyan, right).

(F) Missing-wedge-corrected final denoised map density (NCPs in cyan, SA crystal in pink). This final map was used to generate the fitted model (bottom) (NCPs in blue, 40 bp linker DNA in yellow).

(G) Comparison of the final 3D map (left) and the fitted model (right) of the dashed line area in (C–F).

(H) Local areas showing tetranucleosomes in extended (top panels) and stacked (bottom panels) conformations.

salt buffer (150 mM Na$^+$ and 5 mM Mg^{2+}) on 2D streptavidin (SA) crystal grids (Han et al., 2016) (Figures 1B and S3C). Given the minimum on-grid incubation time of 2 min for biotin binding to SA (Han et al., 2016), we used the low salt (2 min) condition to approximate the earliest (0 min) incubation times of the physiological salt concentration.

We designed a cryo-ET workflow to determine the spatial organization and coordinates of individual NCPs, both free and inside the condensates (Figures 1C–1H). To test our strategy, we began with a sample incubated for 10 min at 4°C in physiological salt. By using deep-learning-based denoising of each tilt image (Buchholz et al., 2019; Weigert et al., 2018) to enhance the low-dose image contrast (Figure 1C), coupled with a focused refinement strategy of individual-particle electron tomography (IPET) (Zhang and Ren, 2012), we successfully obtained 3D density maps and identified NCP clusters displaying low level of condensation (Figures 1D and S4A). The z-dimensional 2D slice of the 3D map revealed the irregular arrangement of NCPs within the condensates (Figure 1E, left panel).

After annotating the initial 3D map using deep-learning-based global segmentation (Chen et al., 2019) (Figures 1E, right panel,

and S4A), we produced a coarse 3D map labeling all NCP positions (Video S1). To regain the molecular details of NCPs, the initial and the coarse labeling 3D maps were superimposed, and the latter was used as a marker to select the surrounding connected map density within the former. The resulting maps were then low-pass filtered and served as a mask for local missing wedge correction (Zhai et al., 2020). This procedure yielded the final denoised 3D map depicting NCPs isolated or in condensates, as well as their flanking DNA (Figures 1F, top panel, and S4A).

Next, flanking DNA and NCP models (PDB: 1AOI) were docked into the final 3D map (Figures 1F, bottom panel) via a weighted iterative search algorithm (see STAR Methods). We evaluated the result of this fitting by both calculating the cross-correlation (cc) score between the local map density and the model and by performing sub-tomogram averaging. On the one hand, we obtained an averaged cc value of ∼0.8 ± 0.1 (Figure S4B; first row, third column), well above the value of ∼0.3 obtained for a control (Figure S4B, right panel). On the other hand, the averaged 3D maps obtained had a resolution of 20–25 Å (estimated at Fourier shell
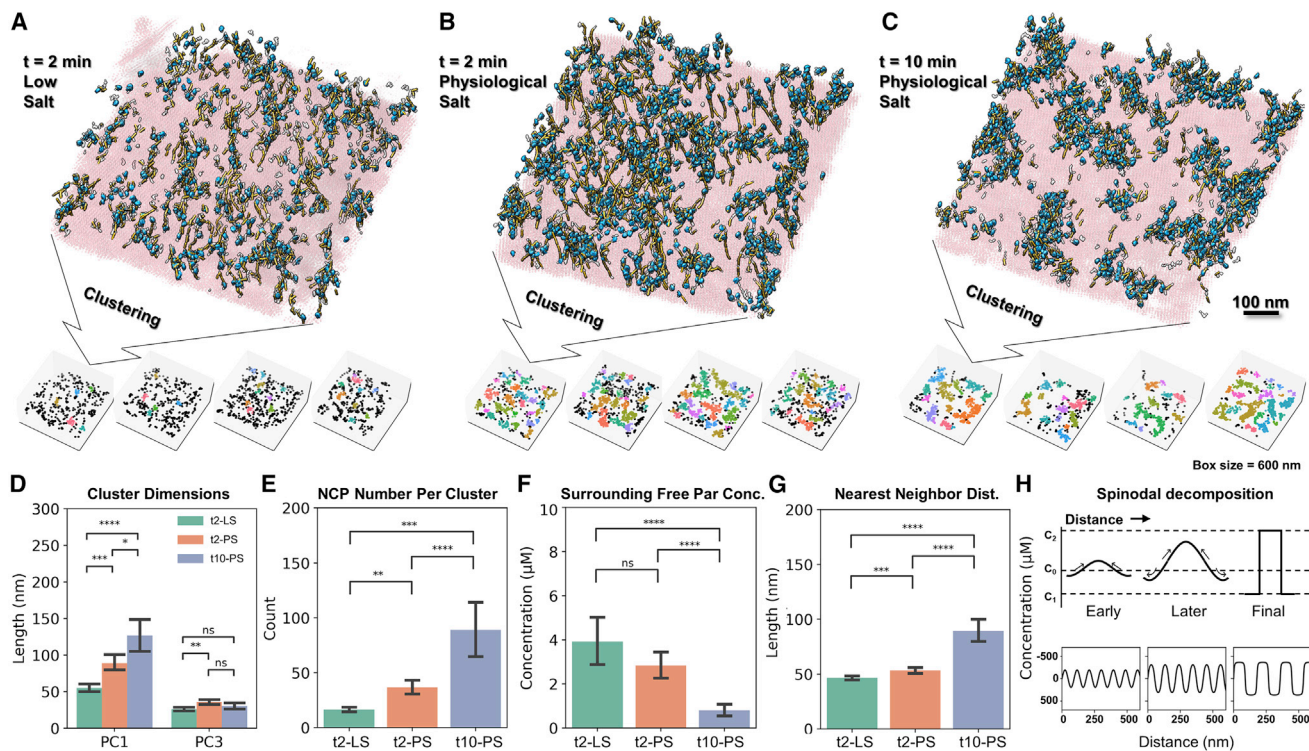
Figure 2. Time evolution of irregular condensates

Final denoised maps (thickness of ~90–130 nm) with fitted models displaying irregular tetranucleosome condensates obtained in low and physiological salt at 4°C.

(A) Top: 2-min incubation at low salt (15 mM Na^+, t2-LS).

(B) Top: 2 min at physiological salt (150 mM Na^+ and 5 mM Mg^{2+}, t2-PS).

(C) Top: 10 min at physiological salt (t10-PS). SA crystal and nucleosome densities are pink and transparent gray, respectively. Fitted NCPs and flanking DNA colored in cyan and yellow, respectively.

Bottom panels for (A), (B), and (C) show NCP clusters of four representative tomograms for each incubation condition, grouped by the density-based spatial clustering of applications with noise (DBSCAN) algorithm. Each color represents a unique NCP cluster and black depicts free, unclustered NCPs.

(D) Condensates' dimensions along PC1 and PC3 axes derived from PCA.

(E) Number of NCP per condensate.

(F) Concentration of free NCPs surrounding a condensate within a 20 nm shell.

(G) NND between condensates. All statistics are plotted as mean ± SEM and compared using a two-tailed unpaired t test, where *p < 0.05, **p < 0.01, ***p < 0.001, ****p < 0.0001, and ns, not significant.

(H) Schematic representation of the spinodal decomposition process as a function of time obtained from the Cahn-Hilliard equation: top, image modified from (Findik, 2013); bottom, evolution of irregular condensates in terms of their NND (wavelength), condensate internal concentration (amplitude), and surrounding free NCP concentration (sharpness) represented by a Squdel sine function.

correlation cutoff at 0.5 and 0.143), which is sufficient to distinguish the ~1.7 turns of DNA wrapped around the histone core (Figure S4C). Thus, the identification of NCPs within the tomogram is robust. The final model and 3D map show the distribution of individual NCPs and DNA components (Figure 1G; Video S2). Two representative 3D zoom-in views of individual tetranucleosome arrays show NCPs and flanking DNA arranged in extended and stacked conformations (Figure 1H; top and bottom panels, respectively). Finally, the models provide the coordinates of individual NCPs.

The early stage of nucleosomal condensation occurs by spinodal decomposition

To characterize the condensates quantitatively, we calculated the space coordinates of the center of mass of individual

NCPs and grouped them using a density-based clustering algorithm (DBSCAN) (Ester et al., 1996). NCPs surrounded by at least twelve NCP neighbors (self-included) within 27–29 nm (see STAR Methods) were classified as clusters or condensates (Figures 2A–2C). Each identified cluster was color coded. NCPs that could not be associated with any cluster were depicted in black and represent "free" NCPs. At 2 min of incubation, 4°C, and 15 mM Na^+, most NCPs appeared dispersed over the field of view, only a few of them were grouped into small clusters (Figure 2A). In sharp contrast, at 2 min of reaction in physiological salt, most NCPs were grouped into larger, irregularly shaped condensates (Figure 2B) that continued to grow after 10 min of reaction (Figure 2C). We propose that the sparse distribution of condensates in 15 mM Na^+ mirrors the earliest stage (0 min) of nucleosome condensation at physiological

CellPress
OPEN ACCESS

salt. Hereinafter, this type of structure will be referred to as the initial state.

The early condensates exhibited irregular, elongated shapes and were densely distributed across the surface. We used principal-component analysis (PCA) (Hotelling, 1933) to quantitatively characterize these condensates by identifying their long (PC1) and short (PC3) axes. The average size of the condensate's long axis at the initial state was 55.1 ± 5.2 nm, and the average size of the short axis was 26.1 ± 2.4 nm. After 2 and 10 min of reaction (4°C and physiological salt), these two values increased to 89.0 ± 10.1 and 35.9 ± 3.0 nm and to 126.9 ± 19.6 and 31.6 ± 4.0 nm, respectively (Figure 2D). This analysis reveals that these clusters grow asymmetrically along their long axes, while the short axes remain nearly constant with a diameter of ∼30 nm. As a result, their eccentricity (defined as 1 − short axis/long axis) increases from 0.51 ± 0.05 to 0.56 ± 0.03 to 0.73 ± 0.03 at initial, 2, and 10 min of reaction time, respectively (Figure S5A). The growth of the condensates is also accompanied by an increase in the average number of NCPs per condensate, from 17 ± 3 to 37 ± 6 to 89 ± 26 (Figure 2E). Next, we quantified the depletion of NCPs around the condensates as the reaction proceeded by determining the number of isolated NCPs found within a 20 nm shell surrounding the condensate (Figure 2F). At the initial state, the concentration of NCPs within the shell was 3.9 ± 1.0 μM; this value decreased to 2.8 ± 0.5 μM after 2 min and to 0.8 ± 0.3 μM after 10 min of condensation reaction (Figure 2F). To further validate this analysis, we determined the total number of free NCPs within the imaged area and calculated their concentration in the ice slab. Consistent with the above results, the concentration of free NCPs decreased from 25.0 ± 3.5, to 8.9 ± 2.3, and 3.9 ± 0.7 μM for the initial state, 2 and 10-min observation time, respectively (Figure S5B). The total (free + condensed) concentration of NCPs within the ice slab throughout the reaction slightly increased from 31.7 ± 5.4, 41.0 ± to 3.7, and to 48.4 ± 16.8 μM (Figure S5C) for the three time points analyzed.

These observations are consistent with a mechanism of spinodal decomposition, which involves negative diffusion of solute materials against a concentration gradient, gradually forming irregular condensates with defined borders. Spinodal decomposition does not involve crossing an energy barrier; therefore, the formation of condensates is ubiquitous and arises because of local, small concentration fluctuations in the medium. The growth of these SpnCs can be described in terms of a time-dependent periodic distance or wavelength λ(t), which gives the average separation between domains of the condensed phase, ultimately attaining a maximum value λ_max (Methods S1, Equation 9) (Emo et al., 2014). The spacing between condensate clusters was estimated by calculating the mean nearest neighbor distance (NND) between condensates using a low-pass-filtered (8 nm) maps (Figure S5E). The average spacing between condensates gradually increased from 46.5 ± 1.8 to 53.3 ± 2.8 to 89.5 ± 9.8 nm at 10 min (Figure 2G). A pairwise correlation test among five independent measurements, i.e., condensate cluster size, eccentricity, number of NCPs per condensate, concentration of surrounding free NCPs, and NND, yielded a mean absolute r value of 0.73 (Figures S5D–S5F). This high correlation confirms that SpnCs grow by asymmetric accretion of isolated NCPs leading to the

formation of elongated structures with sharp borders, according to a spinodal decomposition process (Figure 2H).

Spherical condensates arise by nucleation and growth in the later stages of phase separation

Distinctive, spherically shaped structures with variable sizes from ∼40 to ∼400 nm in diameter appeared scattered among SpnCs after 10 min of incubation at room temperature in physiological salt (Figure 3A; panels I and IV). These condensates appear denser compared with the surrounding irregular spinodal materials, suggesting that they are an early stage of liquid droplets. Their sparse distribution (Figure S6A) is consistent with the existence of an energetic barrier that must be crossed for these condensates to form.

To characterize the internal structure of these SphCs and their relationship to the surrounding SpnCs, we mapped out the NCPs in areas containing both types of structures (Figure 3B). Because our fluorescence data showed that liquid droplets gradually increase their size with time, we ordered representative SphCs (segmented 2D slices and corresponding 3D models) by size to illustrate possible early stages of droplet formation and growth (Figures 3B and 3C; panels I–IV). We also captured fusion events between small and intermediate size SphCs (Figures 3B and 3C; panel I, yellow arrows, and white arrows, respectively). Moreover, our data also indicate that growth of SphCs not only occur by self-fusion but also by accretion of spinodal materials, as reflected by the presence of irregular condensates attached to spherical ones (Figures 3B and 3C; panel II, red arrow). Panel III in Figures 3B and 3C illustrates a possible merging event (purple arrow) of smaller condensates to form a larger one while maintaining their spherical morphology. Such a process suggests a mechanism by which even larger SphCs are generated (∼400 nm) (Figures 3B and 3C; panel IV).

Small SphCs (Figure 3B; panel I, yellow arrows) were comparable in size to their spinodal counterparts but appeared perfectly spherical. We propose that these small SphCs result from an early nucleation step that eventually gives rise to larger condensates. To confirm this inference and capture nucleus formation, we also analyzed samples after 20 min of incubation since nucleation rarely occurs at early times, requiring longer incubation periods (Sear, 2014) (Figure S6B). Under these conditions, we observed more small SphCs (Figures S6C and S6D), either isolated or in groups of two or three (Figures 4A and 4B). Statistical analysis indicates that there is a similar probability of finding isolated small SphCs or clusters of them (Figure 4C). This observation suggests that clusters of SphCs probably arose from a common large local concentration fluctuation within a SpnC.

Closer examination revealed that some small SphCs appeared surrounded by and connected to irregular SpnCs (Figure 4D). Panel I in Figure 4E shows an example in which only half of the condensate was rounded and made up of 28 NCPs, while the other half, with 36 NCPs, was less organized. The total NCP number is comparable to that of late SpnCs (∼60 NCPs) (Figure 4E). These hybrid structures were also detected by OpNS-EM (Figure S1E, white arrow). While in early reaction, SpnCs were present without SphCs, the converse was not true:
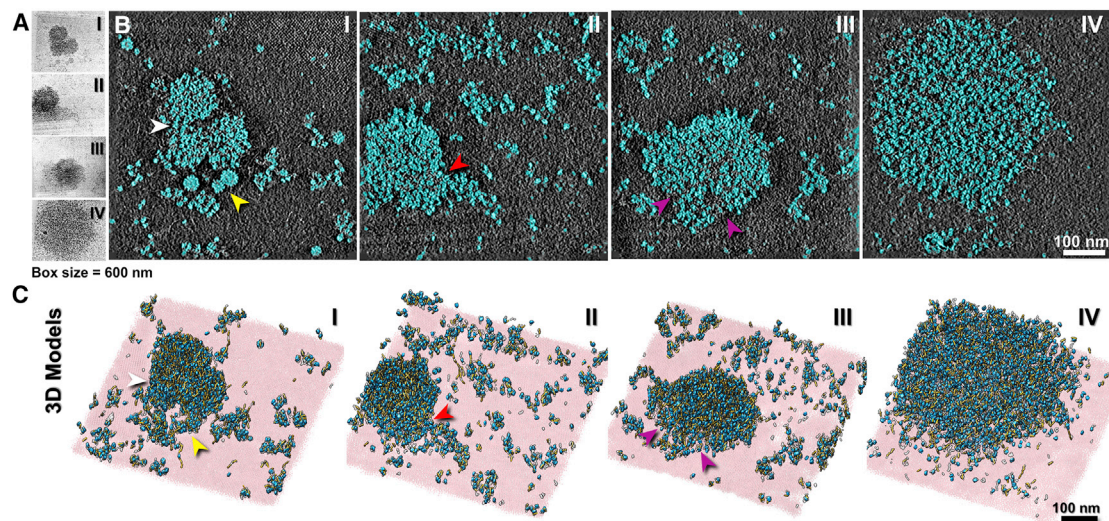
Figure 3. 3D reconstructions of initial stages and growth of spherical condensates
Spinodal condensates (SpnCs) and spherical condensates (SphCs) of different sizes after 10 min incubation of tetranucleosome at 20°C in physiological salt.
(A) Enhanced cryo-ET zero-tilt images from tomograms labeled I–IV, ordered by increasing SphCs size.
(B) Corresponding tomogram slices (1.17 nm thickness) depicting NCPs (cyan) after deep-learning-based segmentation.
(C) Final 3D map of tomograms in (B) showing the NCP (transparent gray) and SA crystal (pink) densities (tomograms thickness ∼90–140 nm). NCP component of the fitted models shown in cyan and the flanking DNA segment in yellow. I–IV illustrate a possible mechanism of growth of SphCs: (I) formation of small, near-spherical condensates (∼35 nm, yellow arrow) and merging of three larger SphCs (∼100 nm, white arrow); (II) accretion of SpnC by a ∼200 nm SphC (red arrow); (III) a ∼300 nm SphC resulting from the apparent fusion (purple arrows) of smaller condensates; (IV) a larger (∼400 nm) SphC resulting from growth processes.

SphCs were only observed among irregular condensates. Together, these observations suggest that the small SphCs emerged from the pre-formed SpnCs and served as nuclei that can then grow into larger SphCs, either via fusion among themselves and/or from accretion of surrounding spinodal structures.

The size distribution of all SphCs in the 2D micrographs revealed two peaks centered at diameters of 60 ± 14 and 161 ± 66 nm, while the smallest structures had a diameter of ∼35 nm (Figure S6E). We suggest that the first peak represents the formation of thermodynamically unstable initial nuclei due to large local concentration fluctuations. The valley between the two peaks might indicate the dimensions beyond which the initial nuclei begin to overcome the interfacial energy barrier to (irreversibly) grow into larger and more stable structures (Figure S6E). The peak at ∼160 nm (Figure S6E) is likely the result of two opposing factors: one favoring the formation of larger condensates by the extra thermodynamic stability gained during growth by accretion of spinodal materials and/or their fusion, and another disfavoring further growth because of the depletion of nearby materials. Note that the smallest spherical nuclei, although tightly packed, also contained regions of randomly located cavities (Figure 4E; top panel, yellow arrows).

Once again, we posit a possible temporal evolution of SphC nuclei growth (Figure 4E; panels I–IV). After the earliest stage in which small unstable nuclei are formed (panel I), they are often seen with either linear or clustered arrangement (panels II and III). It is possible that the latter are favored over the former by lowering the interfacial surface, a process that, upon fusion, will lead to a more favorable (smaller) surface-to-volume ratio. Nonetheless, the high probability of observing clusters composed of unfused spherical nuclei might be due to a second-

ary energy barrier required for nucleus fusion. Larger nucleosome droplets then emerge once this barrier is overcome (panel IV). Taken together, these observations indicate that nucleosome phase separation occurs through a two-step process: the first involves the formation of condensates by spinodal decomposition, followed by the re-organization of those into spherical, tightly packed condensates.

H1 catalyzes the spinodal-to-spherical condensate transition

Linker histone H1 regulates chromatin compaction and packaging (Andreyeva et al., 2017; Song et al., 2014; Zhou et al., 2016). Epifluorescence microscopy revealed that H1 added in a 1:1 ratio to NCPs increased the number and size of nucleosome droplets (Figure 5A). To determine how H1 affects the proposed two-step mechanism, we repeated the OpNS-EM experiments in the presence of H1. We found that H1 significantly accelerates the formation of large micron size SphCs to ∼2 min (Figures S7A–S7D), from the 60 min required in its absence (Figure S1A). Also, in the absence of H1, the surface number density of NCP (measured from areas devoid of SphCs) decreased only by ∼7% after 90 min of incubation (Figure S1B), whereas in the presence of H1, this parameter decreased exponentially to one-third of its initial value during the same time (Figure S7E). At 4°C and 36°C, the process follows a similar trend but at lower rates (20°C > 36°C > 4°C, Figure S7E). This result is consistent with the observation that the rate of SphCs formation does not monotonically depend on the temperature of incubation without H1 (Figure S1B). Interestingly, a similar non-monotonic behavior with temperature has been described for tau protein condensates (Dong et al., 2021).
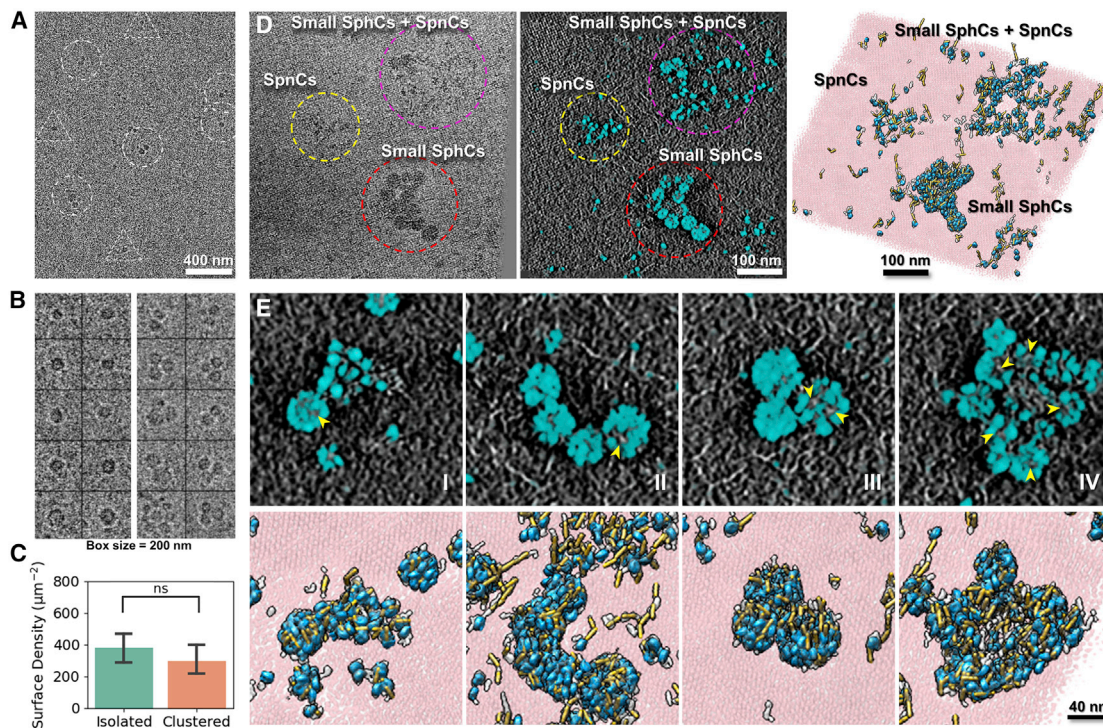
Figure 4. Small spherical nuclei arise from SpnCs

(A) Cryo-EM image showing single (dashed triangles) and multiple (dashed circles) small SphCs formed at 20°C, physiological salt, and 20 min of incubation.

(B) Representative particles of individual (left columns) and clustered (right columns) small SphCs.

(C) Statistics from 12 low-magnification images indicating a similar probability of finding condensates in clusters or in isolation. Data plotted as mean ± SEM. ns, not significant.

(D) High-magnification cryo-ET zero-tilt image (left), tomogram slice (middle), and 3D model (right) of a cluster of small SphCs (red dashed circle), SpnCs (yellow dashed circles), and small SphCs in proximity to SpnCs (magenta dashed circle).

(E) Various stages of the nucleation-and-growth processes (I–IV) of SphCs shown by representative tomographic slices (top) and their corresponding 3D maps and models from ~70 nm thickness tomograms (bottom). The states include: (I) conversion of a SpnC into a small nucleus; (II) formation of multiple nuclei in side-by-side contact; (III) small nuclei organized in a cluster; and (IV) cluster of nuclei with smeared boundaries suggesting a process of fusion. Yellow arrows identify cavities within the small nuclei.

These rapidly forming SphCs were also observed by cryo-ET after 10 min of incubation at 20°C in physiological salt (Figure 5B). Cryo-ET reconstruction (Figures 5C and 5D) reveals that the NCP packing density of these condensates is tighter (panel III) than those formed in the absence of H1 (Figure 3A; panel IV). The central z-dimensional slices and corresponding 3D models display SphCs that appeared to be fusing with other SphCs or accreting spinodal materials (Figures 5C and 5D, yellow arrows). The sparse presence of SpnCs, compared with their larger abundance around SphCs found in the absence of H1 (Figures 3B and 3C), supports our inference that H1 does not prevent the formation of SpnCs but catalyzes their transition to SphCs.

NCP organization inside the spinodal and spherical condensates

The cryo-ET data indicate that SphCs have a higher density and larger diameter than the SpnCs (Figures 2, 3, and 5). In order to further characterize the nucleosomal architecture inside each type of condensate, we used the spatial coordinates of individual NCPs to determine their concentration, inter-nucleosome distance distribution, and orientation. To estimate the NCP concentration, we first defined a series of concentric 3D contours separated by 2 nm, placed at the condensate's center of mass (see details in STAR Methods, Figure 6A; left panel). We then calculated the NCP concentration within contour n (internal volume concentration, Figure 6A; middle panel); the difference of the number of NCPs enclosed by contours n and $n-1$ divided by the difference in their volumes gave us the NCP concentration of shell n (shell concentration, Figure 6A; right panel). Next, we average the concentrations enclosed by successive contours for all condensates of the same type (Figure 6B) and for each shell, starting from $n>5$, as both concentrations are not well defined when the measured volume approaches the size of a single NCP.

For contour $n=6$, the shell concentrations for the initial, intermediate, and late-stage SpnCs were 217 ± 43, 274 ± 36, and 356 ± 66 μM, respectively, and the corresponding internal volume concentrations were 195 ± 25, 309 ± 21, and 364 ± 47 μM (Figure 6C; left column). The shell concentration for all SpnCs stages—initial, intermediate, and late—decreased toward the periphery of the condensates, vanishing at shells $n=17$, 24, and 28, respectively (Figure 6C; left column). In comparison,
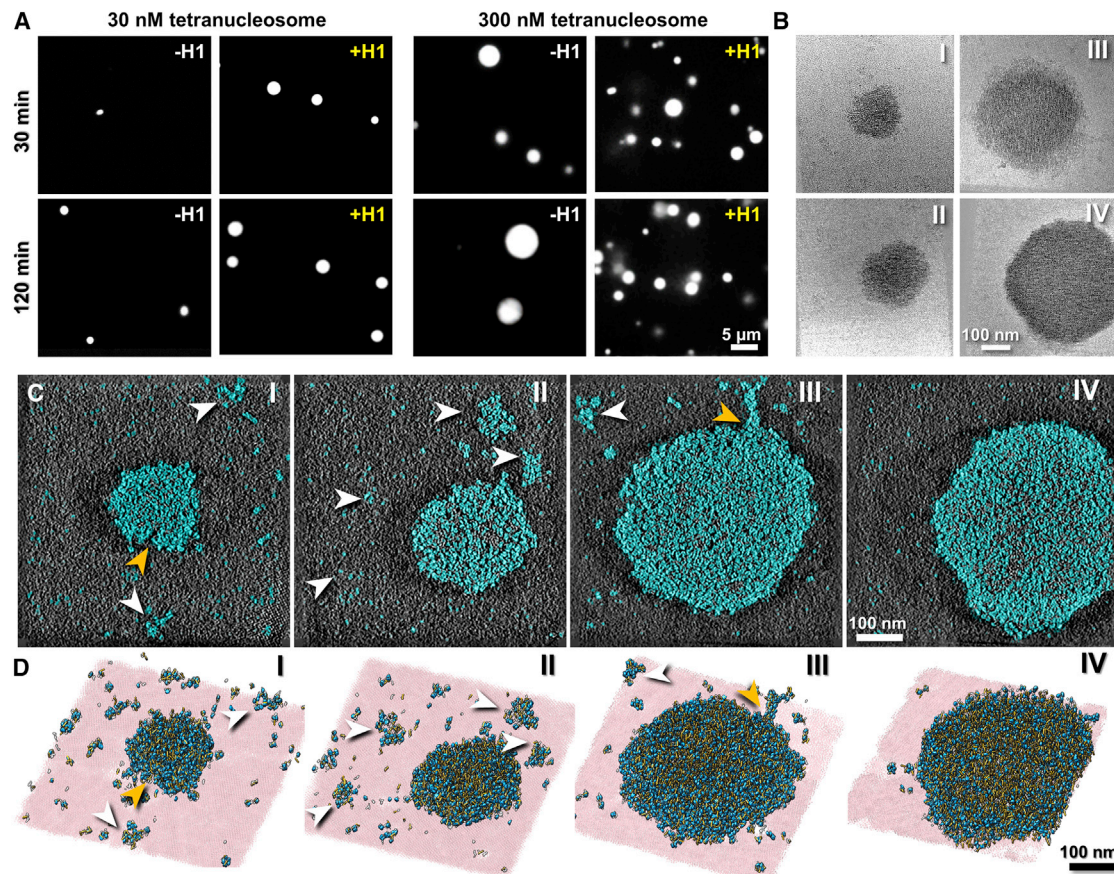
Figure 5. Linker histone H1 accelerates the transition from SpnCs to SphCs

(A) Fluorescence microscopy images of 30 nM (left) and 300 nM (right) Cy3-labeled tetranucleosomes incubated at 20°C in physiological salt with and without H1.

(B) Representative zero-tilt cryo-ET images of SphCs obtained in the presence of H1 at 20°C, physiological salt and 10 min of incubation ordered by increasing size and labeled I–IV.

(C) Tomogram slices corresponding to (B).

(D) 3D maps (tomograms thickness, ~90–130 nm) and models of the corresponding condensates, illustrating various stages of SphCs growth. White arrows indicate the sparsely distributed SpnCs in the surrounding areas. Orange arrows indicate fusion events between condensates.

the initial spherical nuclei, the SphCs, and the SphCs in the presence of H1 (SphCs-H1), all displayed higher shell and internal volume concentrations than their spinodal counterparts. At shell $n = 6$, concentrations are 286 ± 97, 339 ± 74, and 612 ± 152 μM, respectively, and the corresponding internal volume concentrations are 494 ± 68, 402 ± 45, and 550 ± 138 μM (Figure 6C; right column). Unlike SpnCs, all three types of SphCs—nuclei, SphC, and SphC-H1—displayed a slight increase in shell concentrations toward the periphery reaching a peak shell concentration of 939 ± 99, 501 ± 36, and 688 ± 65 μM, and a peak internal volume concentration of 743 ± 64, 471 ± 42, and 667 ± 62 μM, respectively (Figure 6C; right column). Thus, the NCP concentration in SphCs is ~1.3- to 3.6-fold higher than that in the SpnCs and increase significantly in the presence of H1. The large discrepancy between the peak shell and peak volume concentrations (~200 μM) observed in spherical nuclei suggests that the formation of a nucleus involves an outer shell of tightly packed NCPs but an interior somewhat more loosely organized, as highlighted in Figures 4D and 4E.

Next, we calculated radial distribution functions g(r) around each NCP and averaged them over all condensates of the same type (see STAR Methods). This analysis reveals two characteristic peaks residing at distances of ~8 and ~21 nm (Figure 6D, dash lines). The first peak, which corresponds to the distance between nearest NCPs centers, moves from 7.5 to 8.1, and to 9.0 nm for the initial, intermediate, and late SpnCs, respectively. The value of 7.5 nm can be rationalized as the distance between two NCPs averaged from their various contact conformations: the side-by-side conformation adopted by NCPs belonging to neighboring arrays and the stacking conformation of i and $i + 2$ NCPs within the same array yielding the maximum and minimum core-to-core distance of 11 and 5.5 nm, respectively (Figure 6E; left panel). The rest of the NCPs' contact conformations should contribute to distances that lie somewhere in between the above two extremes (Bilokapic et al., 2018). The small shift in the peak distance as the SpnCs mature and grow might reflect a decrease in the statistical weight of intra-array $i/i + 2$ stacking in favor of inter-array
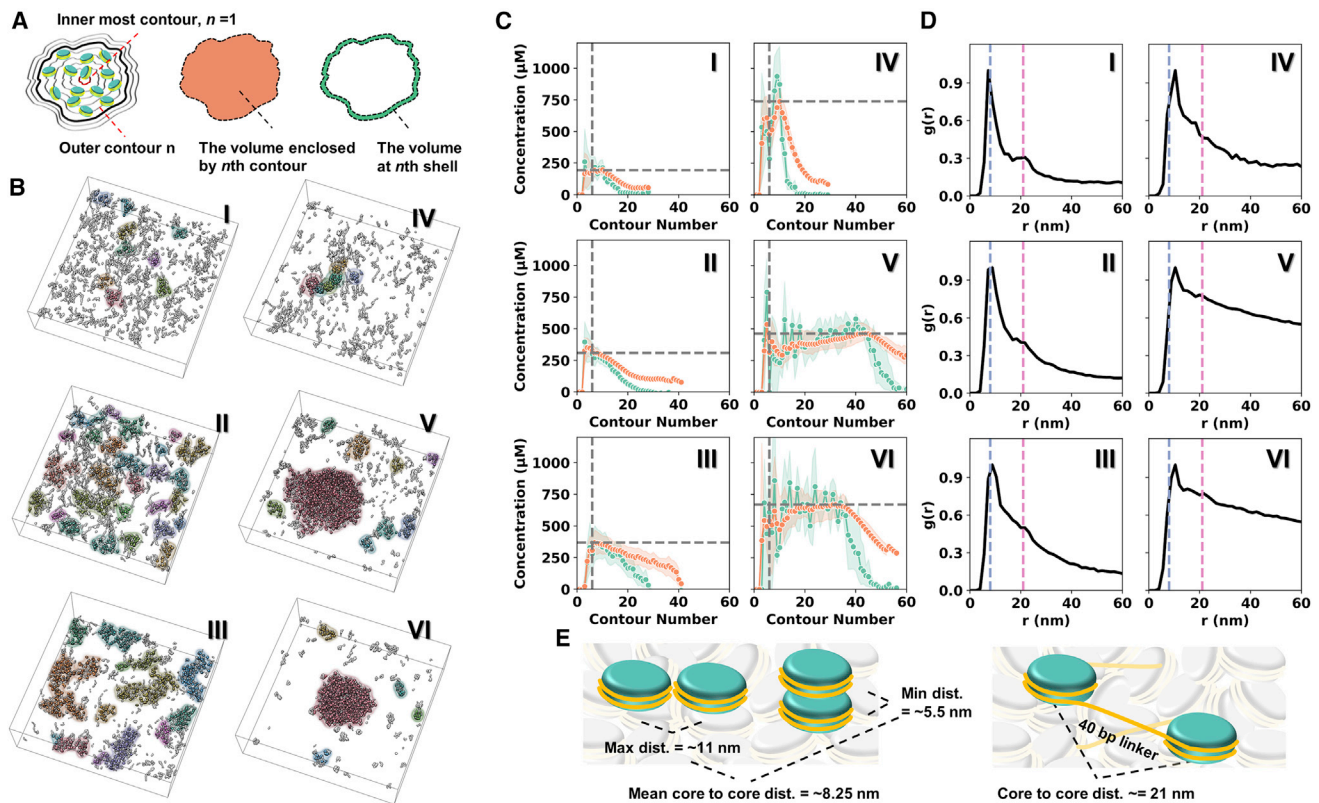
CellPress
OPEN ACCESS

Figure 6. Quantitative analysis of NCP concentration and organization throughout condensate growth

(A) Schematic representation of a series of condensate-shaped concentric contours (2 nm apart, left), volume enclosed by the nth contour (orange, middle) and volume delimited by contours n and $n − 1$ (green, right). Internal volume and shell concentrations are calculated as described in the text.

(B) The shape of the condensate was defined by 10 nm low-pass maps shown in different colors. The numbering of the maps follows the order from early (I), intermediate (II), and late-stage (III) SpnCs to the small nuclei (IV) and larger SphCs without (V) and with (VI) H1. Box size = 600 × 600 × 230 nm.

(C) Quantification of the nth-internal volume (orange) and nth-shell (green) NCP concentration corresponding to stages I through VI. Horizontal dashed lines mark the highest volume concentration beyond $n = 5$ (vertical dashed lines).

(D) Radial distribution function g(r) of NCPs' centers of mass for stages I through VI. Blue and pink dashed lines indicate two characteristic nucleosome's core-to-core distances at 8 and 21 nm, respectively.

(E) Theoretical inter-nucleosome distances for side-to-side (11 nm) and stacked (5.5 nm) configurations (left), and intra-nucleosome distance between neighboring NCPs within an array (21 nm, right).

interactions. Similarly, the spherical nuclei, SphCs, and SphCs-H1 also display a first peak shift toward higher values of 10.6, 10.5, and 10.6 nm, respectively (Figure 6D, blue dash line); perhaps the higher compaction in SphCs further discourages intra-array $n/n + 2$ stacking in favor of inter-array NCPs interactions, a hypothesis supported by *in silico* simulations (Farr et al., 2021). The second peak (Figure 6D, pink dashed line) appears as a shoulder, matching the distance expected between i and $i + 1$ NCPs that are connected by a 40 bp DNA linker in every array (Figure 6E; right panel). The monotonic decrease in the amplitude of this peak from early SpnCs to grown SphCs may reflect the bending of the linker DNA within an array, and/or the increased statistical weight of neighboring NCPs belonging to different arrays as a result of the condensation process. Overall, the high-density SphCs have a slower g(r) decay indicating a higher chance to find neighbor NCPs at a close distance compared to with early SpnCs, consistent with the concentration measurements.

The spherical shape of nuclei suggest that the formation of these structures involves unfavorable nucleosome surface-water interactions. Accordingly, we investigated whether the orientation of NCPs on the surface of these condensates differs from those in the interior (see STAR Methods). If the NCP disks are randomly distributed, the probability density distribution of their angular orientation should follow a cosine distribution, $P(\theta)d\theta = \cos(\theta)d\theta$ (see STAR Methods). Deviation from this distribution indicates a preferential orientation of the NCP disks either on the surface or in the interior of the condensates. The results of this analysis (Figures S8A–S8C) showed that the NCPs in the interior exhibited very small deviations from a random distribution, both in SpnCs and in SphCs with or without H1. Only NCPs within the initial spherical nuclei displayed a moderately skewed angle distribution, where the disks tended to orient more parallel to the condensates' surface. In contrast, the NCPs at the surface of SpnCs, SphCs, and SphCs-H1 showed a slightly increased tendency to align perpendicular to the condensate surface ($\theta = 0$).
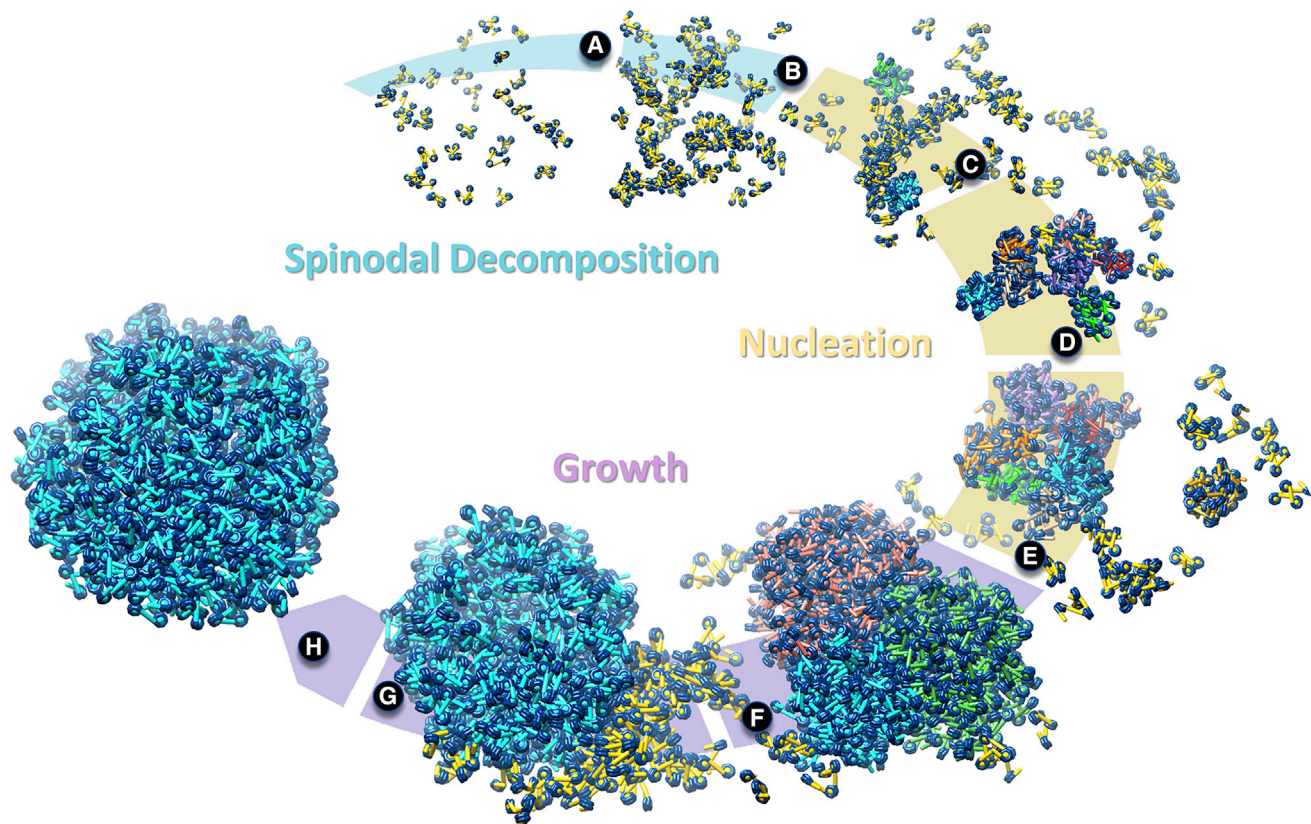
Figure 7. Proposed two-step mechanism of nucleosome phase separation

(A) Initial, dispersed phase of tetranucleosome arrays.

(B) Organization of tetranucleosomes into irregular SpnCs.

(C) Spherical nuclei emerging inside the spinodal phase and growing by addition of neighboring spinodal material.

(D) Bundle of spherical nuclei.

(E) Fusion of nuclei bundles enables growth into larger, energetically stable SphCs.

(F) Fusion of SphCs.

(G) Growth of SphCs by accretion of surrounding spinodal materials.

(H) Large SphC corresponding to the early stage of liquid droplets.

Light blue, pale brown, and purple background indicate the major steps of nucleosome condensation: spinodal decomposition, spherical nuclei formation, and growth of SphCs, respectively. H1 catalyzes steps (C–H). SpnCs are in yellow, and SphCs are multicolored. All states are illustrated with experimentally observed condensates.

Once again, only in the initial nuclei, the NCPs at the surface tended to align parallel to the condensates' surface ($\theta = \pi/2$). Thus, the energetic and global structural differences between SpnCs and SphCs do not arise from a distinct spatial arrangement of NCPs within them. Instead, the transition between these two condensed forms must involve a change in the nature of the inter-nucleosome and nucleosome-solvent interactions.

DISCUSSION

Using cryo-ET, we have captured for the first time the 3D molecular organization of tetranucleosome arrays during the initial stages of their phase separation, when condensates are only a few tens of nanometers in size. We obtained snapshots of condensates at different incubation times in physiological salt, from which it has been possible to infer their likely process of growth and maturation. We find that nucleosome phase transition oc-

curs through a two-step mechanism (Figure 7; Video S3). In the first step, dispersed nucleosomes (at 120 nM concentration) experience a fast system-wide condensation resulting in the ubiquitous appearance of irregularly shaped clusters. These condensates attain an NCP concentration of ~360 µM and average dimensions of (~125 nm × 65 nm × 30 nm). During their formation, they grow by enlarging their major axis, while their minor axes remain nearly constant. This step closely resembles a spinodal decomposition process in which aggregate formation occurs throughout the system without the crossing of an energy barrier. The condensates' anisotropic morphology has been described as a characteristic feature of spinodal processes at early times resulting from diffusion effects, and with isotropy regained at longer times driven by hydrodynamic effects (Datt et al., 2015). According to the Cahn-Hilliard theory of spinodal decomposition (Methods S1), the distance among the resulting SpnCs is determined by a "critical wavelength

Molecular Cell
Article

CellPress
OPEN ACCESS

λ" that describes the spatial pattern of separation between the two phases.

In the second step, the system undergoes a second condensation process in which highly packed spherical nuclei emerge locally and sparsely from the existing SpnCs. This step resembles a more traditional nucleation-and-growth process in which an initially unfavorable event (nucleation) is increasingly stabilized by a favorable volume energy through gaining NCP-NCP interactions distinct to those adopted in the SpnCs. These new inter-nucleosomal interactions must be accompanied, however, by an unfavorable surface energy with the solvent, which forces the system to adopt a spherical shape and minimize its surface-to-volume ratio. Throughout their growth, the initial small and unstable nuclei become increasingly stabilized through a process of accretion of the surrounding spinodal materials, or by fusion with other spherical nuclei. We identify that the phase separation described here is a two-step process—as opposed to a simple spinodal phase that undergoes coarsening or Ostwald ripening (Ostwald, 1897) because we observed a clear separation of timescales between the formation of the two phases. The spinodal decomposition achieves a steady state before 10, 2, and 10 min for the 4°C, 20°C, and 36°C reaction, respectively (indicated by the arrested growth of condensates' dimensions, Figure S1A), while the nucleation process was observed after 60, 2, and 10 for reactions at 4°C, 20°C, and 36°C, respectively (Figure S1B). In contrast, a process of Ostwald ripening will occur continuously, with the formation of the matured SpnCs without a clearly defined timescale separation from the initial spinodal phase and without a nucleation step. This two-step process represents the most parsimonious description of our observations.

The 3D mapping of NCPs reveals that the small nuclei involve a tight packing of a large number of NCPs within a spherical volume as small as ~35 nm in diameter, attaining an NCP concentration of ~740 μM. The sparse appearance of these spherical nuclei at the beginning suggests that their formation is both kinetically and thermodynamically inaccessible from the initial solution of nucleosome arrays and that they only arise from the pre-existing SpnCs as a result of rare, large local concentration fluctuations capable of overcoming a significant energy barrier. Given the localized and rare appearance of these nuclei, it is somewhat surprising that we often observe them close together forming clusters. It is statistically unlikely that these condensates arose at widely separate loci in the medium and came together to form a bundle. Instead, it is more likely that large, localized concentration fluctuations gave rise to multiple nucleation sites at a given location. As these nuclei grow by accretion or fusion, their initial cores must rearrange so that the resulting SphCs display a decreased concentration (~470 μM).

The transition from SpnC to larger SphC does not involve a significant difference in the orientation of NCPs relative to one another or to the outer surface of the condensates. Therefore, this transition with 1.3-fold increase in NCP concentration and a spherical re-organization must involve a qualitative change in the interaction of the NCPs among themselves and with the solvent. Thus, we propose a model in which, in the spinodal process, the condensates retain significant amount of solvent, and the contacts of NCPs among themselves and with the solvent are mediated by polar interactions. These condensates do not

experience a surface energy cost, as the difference between NCP-NCP interactions in the interior and on the surface are not qualitatively different, only quantitatively so, as revealed by their angular orientation. During the nucleation step, in contrast, the solvent must be significantly excluded, and it is likely that hydrophobic nucleosome surfaces are exposed and mediate the NCP-NCP and NCP-solvent interactions. Indeed, it has been reported that Swi6, an HP1-family protein in *S. pombe*, induces LLPS of NCPs by promoting conformational changes that increase the solvent accessibility and dynamics of hydrophobic residues isoleucine, leucine, and valine of the octamer core (Sanulli et al., 2019). Hence, the authors proposed that nucleosome's plasticity is key for the action of Swi6 favoring nucleosomal states that promote LLPS by increasing multivalent interactions between NCPs. Other authors have also emphasized the relevance of hydrophobic residues as adhesive elements in LLPS (Alberti et al., 2019). For example, 1,6-hexanediol (which inhibits weak hydrophobic interactions) causes a more uniformed chromatin distribution in cells (Ulianov et al., 2021) and increases chromatin accessibility (Henikoff et al., 2020). We propose that these exposed surfaces are thermodynamically favorable in the condensates' interior, but unfavorable at their surface, forcing the condensates to minimize the area exposed to the solvent by adopting spherical shapes. Interestingly, the isotropic distribution of the NCPs disks observed in the SpnCs and in the larger stabilized SphCs shows that these condensates are not organized as a solid but as a liquid-like state.

A two-step phase separation pathway to form large spherical droplets, as opposed to a conventional one-step (classical) nucleation mechanism, has precedence in the literature. For instance, phase separation of inorganic nanogold particles, Fe-Mn alloys, as well as in biological ones, such as ferritin (Houben et al., 2020; Kwiatkowski da Silva et al., 2018; Loh et al., 2017a).

During the cell cycle, chromatin exhibits different levels of compaction. The internal NCP concentration of the irregular SpnCs ranges from ~195 to ~360 μM, larger than the estimated chromatin concentration at interphase (80–110 μM) (Hihara et al., 2012). However, when we consider the characteristic spacing λ among SpnCs, we obtain an NCP concentration similar to the interphase value. Interestingly, the average of the short axis length (~30 nm) in SpnCs suggests that nucleosome arrays tend to spontaneously self-assemble into structures with similar dimensions to those described as irregular (Cai et al., 2018b), short-range helical (Scheffer et al., 2011), and regular ladder-like or regular helical shapes (Garcia-Saez et al., 2018; Grigoryev et al., 2009; Robinson and Rhodes, 2006; Song et al., 2014). We found regularly structured condensates very rarely compared with the dominant irregular spinodal morphologies (Figure S1E; left column second row). It is possible that this tendency of tetra-nucleosomes to form SpnCs furnishes the physical basis to a recent model for interphase chromatin organization in which the 10-nm fibers self-interact and condense to generate a polymer-melt structure (Hansen et al., 2018).

The transition from spinodal-to-spherical condensates involves a 1.3-fold increase in NCP concentration (~470 μM, Figure 6), which is in the range estimated for metaphase chromosomes (Hihara et al., 2012) and close to the concentrations

CellPress
OPEN ACCESS

Molecular Cell
Article

predicted by Monte Carlo simulations (~500 μM) (Maeshima et al., 2016). It is interesting to estimate how an increase in NCP concentration affects the ability of a molecule such as RNA polymerase II (MW = 550 kDa) to diffuse inside the condensates, given that the flanking DNA segments of the arrays appear to be hidden inside the SphCs. Empty chamber evaluation analysis (Figure S8D) shows that concomitant to the increase of internal NCP concentration, there is a nearly 10-fold decrease in the number of Pol II molecules that can fit in the late-stage SpnC, SphC, or SphC-H1. This analysis indicates that SphCs, particularly SphCs-H1, would strongly repress transcription initiation by sterically hindering the access and mobility of large transcription pre-initiation complexes. Small molecules, however, could still diffuse inside liquid droplets. Indeed, linker DNA within the liquid droplets can be readily cleaved by micrococcal nuclease (17 kDa) (Maeshima et al., 2016) and by Cas12 (120 kDa) (Strohkendl et al., 2021). Similarly, Tet Repressor (23 kDa) was shown to be strongly recruited into nucleosome droplets in the presence of its operator (Gibson et al., 2019).

Formation of the early spherical nuclei requires at least 10 min of reaction and produces ~2-fold increase in local NCP concentration (~740 μM). This observation suggests that the transition from SpnCs to SphCs is the rate-limiting step in the formation of LLPS, making it a possible target of regulation. Indeed, we find that incubation of nucleosome arrays with H1 catalyzes the formation of SphCs at the expense of the surrounding spinodal materials (Figure 5). It is not possible at this point to state whether or not the transition from SpnCs to SphCs takes place *in vivo*, with H1 and other protein factors reducing the energy barrier for the transition to take place. If that were the case, other protein factors and histone modifications would be required to maintain an open chromatin state during interphase. For example, binding of FoxO1 to nucleosomes induces chromatin opening (Hatta and Cirillo, 2007) and histone acetylation and can disrupt chromatin droplets (Gibson et al., 2019). Future structural as well as complementary methods with better time resolution will be implemented to elucidate how histone acetylation, methylation, and histone tails affect the early stages of spinodal condensation and spherical nuclei formation.

Collectively, it is tempting to extrapolate our *in vitro* observations and propose that in the cell, chromatin can exist in an equilibrium between a loosely packed state (like SpnCs), which would be accessible for transcription, repair, and replication, and a highly packed transcriptionally repressed state (resembling SphCs). In this scenario, cell identity and differentiation could be established through a tight spatiotemporal regulation of the interconversion between these two chromatin forms and explain how physiological homeostasis could be attained in response to external cues.

Limitations of the study

The cryo-ET methodology is suitable to the study of small condensates with a maximum size in the range of 100–200 nm diameter. This limitation imposed by the thickness of the ice slab in the cryo-EM sample preparation. SphCs larger than this limit would likely be distorted in the blotting process causing the formation of cylindrical shape condensates between the air-water interface and the SA crystal surface.

STAR★METHODS

Detailed methods are provided in the online version of this paper and include the following:

- KEY RESOURCES TABLE
- RESOURCE AVAILABILITY
  - Lead contact
  - Materials availability
  - Data code and availability
- METHOD DETAILS
  - Purification of histones proteins
  - Fluorescence labeling of H2A
  - Histone octamer reconstitution
  - Synthesis of tetranucleosome and dodecamer array DNA templates
  - Synthesis of biotinylated tetranucleosome and dodecamer arrays
  - *In vitro* reconstitution of tetranucleosome and dodecamer arrays
  - Atomic force microscopy of nucleosome arrays
  - Tetranucleosome phase transition visualized by epifluorescence microscopy
  - Fluorescence recovery after photobleaching (FRAP) of tetranucleosomes
  - Nucleosome array phase transition visualized by OpNS-EM
  - Preparation of streptavidin 2D crystal grids and cryo-EM sample deposition
  - Cryo-ET data acquisition
  - Deep learning-based denoising
  - Preprocessing of cryo-ET tilt series
  - Cryo-ET 3D reconstruction and NCPs segmentation
  - Missing wedge correction of 3D density map reconstruction
  - Modelling of the final denoised 3D electron density map
- QUANTIFICATION AND STATISTICAL ANALYSIS
  - Identification of free and condensed NCPs
  - Calculation of tetranucleosome condensates geometry
  - Calculation of NCP condensate boundary sharpness
  - Determination of NCP concentration in condensates
  - Calculation of the pair distribution function ($g(r)$) of NCPs within condensates
  - Calculation of the NCPs orientation within condensates

Molecular Cell
Article

CellPress
OPEN ACCESS

AUTHOR CONTRIBUTIONS

DECLARATION OF INTERESTS

SUPPORTING CITATIONS

The following references appear in the Supplemental Information: Cahn and Hillard (1958); Cahn and Hillard (1959); Clerc and Cleary (1995); Erdemir et al. (2009); Ji et al. (2007); Karthika et al. (2016); Kim et al. (2016); Lee et al. (2014); Pong et al. (2007); Schmelzer et al. (2004); Shin and Brangwynne (2017); Thanh et al. (2014); Vekilov (2010); Yau and Vekilov (2001).

REFERENCES

Alberti, S., Gladfelter, A., and Mittag, T. (2019). Considerations and challenges in studying liquid-liquid phase separation and biomolecular condensates. Cell 176, 419–434.

Andreyeva, E.N., Bernardo, T.J., Kolesnikova, T.D., Lu, X., Yarinich, L.A., Bartholdy, B.A., Guo, X., Posukh, O.V., Healton, S., Willcockson, M.A., et al. (2017). Regulatory functions and chromatin loading dynamics of linker histone H1 during endoreplication in Drosophila. Genes Dev. 31, 603–616.

Banani, S.F., Lee, H.O., Hyman, A.A., and Rosen, M.K. (2017). Biomolecular condensates: organizers of cellular biochemistry. Nat. Rev. Mol. Cell Biol. 18, 285–298.

Bancaud, A., Huet, S., Daigle, N., Mozziconacci, J., Beaudouin, J., and Ellenberg, J. (2009). Molecular crowding affects diffusion and binding of nuclear proteins in heterochromatin and reveals the fractal organization of chromatin. EMBO J. 28, 3785–3798.

Belmont, A.S., and Bruce, K. (1994). Visualization of G1 chromosomes: a folded, twisted, supercoiled chromonema model of interphase chromatid structure. J. Cell Biol. 127, 287–302.

Bilokapic, S., Strauss, M., and Halic, M. (2018). Cryo-EM of nucleosome core particle interactions in trans. Sci. Rep. 8, 7046.

Boeynaems, S., Alberti, S., Fawzi, N.L., Mittag, T., Polymenidou, M., Rousseau, F., Schymkowitz, J., Shorter, J., Wolozin, B., Van Den Bosch, L., et al. (2018). Protein phase separation: A new phase in cell biology. Trends Cell Biol. 28, 420–435.

Bowman, G.D., and Poirier, M.G. (2015). Post-translational modifications of histones that influence nucleosome dynamics. Chem. Rev. 115, 2274–2295.

Brangwynne, C.P., Eckmann, C.R., Courson, D.S., Rybarska, A., Hoege, C., Gharakhani, J., Jülicher, F., and Hyman, A.A. (2009). Germline P granules are liquid droplets that localize by controlled dissolution/condensation. Science 324, 1729–1732.

Buchholz, T.O., Krull, A., Shahidi, R., Pigino, G., Jékely, G., and Jug, F. (2019). Content-aware image restoration for electron microscopy. Methods Cell Biol. 152, 277–289.

Cahn, J.W., and Hilliard, J.E. (1958). Free energy of a nonuniform system. I. Interfacial free energy. J. Chem. Phys. 28, 258–267.

Cahn, J.W., and Hilliard, J.E. (1959). Free energy of a nonuniform system. III. Nucleation in a two-component incompressible fluid. J. Chem. Phys. 31, 688–699.

Cai, S., Böck, D., Pilhofer, M., and Gan, L. (2018a). The in situ structures of mono-, di-, and trinucleosomes in human heterochromatin. Mol. Biol. Cell 29, 2450–2457.

Cai, S.J., Song, Y.J., Chen, C., Shi, J., and Gan, L. (2018b). Natural chromatin is heterogeneous and self-associates in vitro. Mol. Biol. Cell 29, 1652–1663.

Chandradoss, S.D., Haagsma, A.C., Lee, Y.K., Hwang, J.H., Nam, J.M., and Joo, C. (2014). Surface passivation for single-molecule protein studies. J. Vis. Exp.

Chen, M., Bell, J.M., Shi, X., Sun, S.Y., Wang, Z., and Ludtke, S.J. (2019). A complete data processing workflow for cryo-ET and subtomogram averaging. Nat. Methods 16, 1161–1168.

Chen, M., Dai, W., Sun, S.Y., Jonasch, D., He, C.Y., Schmid, M.F., Chiu, W., and Ludtke, S.J. (2017). Convolutional neural networks for automated annotation of cellular cryo-electron tomograms. Nat. Methods 14, 983–985.

Clerc, D.G., and Cleary, D.A. (1995). Spinodal decomposition as an interesting example of the application of several thermodynamic principles. J. Chem. Educ. 72, 112.

Datt, C., Thampi, S.P., and Govindarajan, R. (2015). Morphological evolution of domains in spinodal decomposition. Phys. Rev. E Stat. Nonlin. Soft Matter Phys. 91, 010101.

Ding, X., Lin, X., and Zhang, B. (2021). Stability and folding pathways of tetranucleosome from six-dimensional free energy surface. Nat. Commun. 12, 1091.

Dong, X., Bera, S., Qiao, Q., Tang, Y., Lao, Z., Luo, Y., Gazit, E., and Wei, G. (2021). Liquid-liquid phase separation of Tau protein is encoded at the monomeric level. J. Phys. Chem. Lett. 12, 2576–2586.

Eltsov, M., Grewe, D., Lemercier, N., Frangakis, A., Livolant, F., and Leforestier, A. (2018). Nucleosome conformational variability in solution and in interphase nuclei evidenced by cryo-electron microscopy of vitreous sections. Nucleic Acids Res. 46, 9189–9200.

Eltsov, M., Maclellan, K.M., Maeshima, K., Frangakis, A.S., and Dubochet, J. (2008). Analysis of cryo-electron microscopy images does not support the existence of 30-nm chromatin fibers in mitotic chromosomes in situ. Proc. Natl. Acad. Sci. USA 105, 19732–19737.

Emo, J., Pareige, C., Saillet, S., Domain, C., and Pareige, P. (2014). Kinetics of secondary phase precipitation during spinodal decomposition in duplex stainless steels: A kinetic Monte Carlo model – Comparison with atom probe tomography experiments. J. Nucl. Mater. 451, 361–365.

Ercius, P., Alaidi, O., Rames, M.J., and Ren, G. (2015). Electron tomography: A three-dimensional analytic tool for hard and soft materials research. Adv. Mater. 27, 5638–5663.

Erdel, F., and Rippe, K. (2018). Formation of chromatin subcompartments by phase separation. Biophys. J. 114, 2262–2270.

Erdemir, D., Lee, A.Y., and Myerson, A.S. (2009). Nucleation of crystals from solution: classical and two-step models. Acc. Chem. Res. 42, 621–629.

Ester, M., Kriegel, H.-P., Sander, J., and Xu, X. (1996). A density-based algorithm for discovering clusters in large spatial databases with noise. In KDD-96 Proceedings.

CellPress
OPEN ACCESS

Molecular Cell
Article

Farr, S.E., Woods, E.J., Joseph, J.A., Garaizar, A., and Collepardo-Guevara, R. (2021). Nucleosome plasticity is a critical element of chromatin liquid–liquid phase separation and multivalent nucleosome interactions. Nat. Commun. *12*, 2883.

Fernández, J.J., Li, S., and Crowther, R.A. (2006). CTF determination and correction in electron cryotomography. Ultramicroscopy *106*, 587–596.

Finch, J.T., and Klug, A. (1976). Solenoidal model for superstructure in chromatin. Proc. Natl. Acad. Sci. USA *73*, 1897–1901.

Findik, F. (2013). Modulated (spinodal) alloys. Periodicals of Engineering and. Natural Sciences (PEN), 1.

Garcia-Saez, I., Menoni, H., Boopathi, R., Shukla, M.S., Soueidan, L., Noirclerc-Savoye, M., Le Roy, A., Skoufias, D.A., Bednar, J., Hamiche, A., et al. (2018). Structure of an H1-bound 6-nucleosome array reveals an untwisted two-start chromatin fiber conformation. Mol. Cell *72*, 902–915.e7.

Gibson, B.A., Doolittle, L.K., Schneider, M.W.G., Jensen, L.E., Gamarra, N., Henry, L., Gerlich, D.W., Redding, S., and Rosen, M.K. (2019). Organization of chromatin by intrinsic and regulated phase separation. Cell *179*, 470–484.e21.

Grigoryev, S.A., Arya, G., Correll, S., Woodcock, C.L., and Schlick, T. (2009). Evidence for heteromorphic chromatin fibers from analysis of nucleosome interactions. Proc. Natl. Acad. Sci. USA *106*, 13317–13322.

Han, B.G., Watson, Z., Kang, H., Pulk, A., Downing, K.H., Cate, J., and Glaeser, R.M. (2016). Long shelf-life streptavidin support-films suitable for electron microscopy of biological macromolecules. J. Struct. Biol. *195*, 238–244.

Hansen, J.C., Connolly, M., McDonald, C.J., Pan, A., Pryamkova, A., Ray, K., Seidel, E., Tamura, S., Rogge, R., and Maeshima, K. (2018). The 10-nm chromatin fiber and its relationship to interphase chromosome organization. Biochem. Soc. Trans. *46*, 67–76.

Hatta, M., and Cirillo, L.A. (2007). Chromatin opening and stable perturbation of core histone:DNA contacts by FoxO1. J. Biol. Chem. *282*, 35583–35593.

Henikoff, S., Henikoff, J.G., Kaya-Okur, H.S., and Ahmad, K. (2020). Efficient chromatin accessibility mapping in situ by nucleosome-tethered tagmentation. eLife *9*.

Hihara, S., Pack, C.G., Kaizu, K., Tani, T., Hanafusa, T., Nozaki, T., Takemoto, S., Yoshimi, T., Yokota, H., Imamoto, N., et al. (2012). Local nucleosome dynamics facilitate chromatin accessibility in living mammalian cells. Cell Rep. *2*, 1645–1656.

Hotelling, H. (1933). Analysis of a complex of statistical variables into principal components. J. Educ. Psychol. *24*, 417–441.

Houben, L., Weissman, H., Wolf, S.G., and Rybtchinski, B. (2020). A mechanism of ferritin crystallization revealed by cryo-STEM tomography. Nature *579*, 540–543.

Hubstenberger, A., Courel, M., Bénard, M., Souquere, S., Ernoult-Lange, M., Chouaib, R., Yi, Z., Morlot, J.B., Munier, A., Fradet, M., et al. (2017). P-body purification reveals the condensation of repressed mRNA regulons. Mol. Cell *68*, 144–157.e5.

Hyman, A.A., Weber, C.A., and Jülicher, F. (2014). Liquid-liquid phase separation in biology. Annu. Rev. Cell Dev. Biol. *30*, 39–58.

Imai, R., Nozaki, T., Tani, T., Kaizu, K., Hibino, K., Ide, S., Tamura, S., Takahashi, K., Shribak, M., and Maeshima, K. (2017). Density imaging of heterochromatin in live cells using orientation-independent-DIC microscopy. Mol. Biol. Cell *28*, 3349–3359.

Ji, X., Song, X., Li, J., Bai, Y., Yang, W., and Peng, X. (2007). Size control of gold nanocrystals in citrate reduction: the third role of citrate. J. Am. Chem. Soc. *129*, 13939–13948.

Jordan, M.A., Diener, D.R., Stepanek, L., and Pigino, G. (2018). The cryo-EM structure of intraflagellar transport trains reveals how dynein is inactivated to ensure unidirectional anterograde movement in cilia. Nat. Cell Biol. *20*, 1250–1255.

Karthika, S., Radhakrishnan, T.K., and Kalaichelvi, P. (2016). A review of classical and nonclassical nucleation theories. Cryst. Growth Des. *16*, 6663–6681.

Kim, J., Lee, S., Choi, Y., Lee, S.-M., and Jeong, D. (2016). Basic principles and practical applications of the Cahn–Hilliard equation. Math. Probl. Eng. *2016*, 1–11.

Kremer, J.R., Mastronarde, D.N., and McIntosh, J.R. (1996). Computer visualization of three-dimensional image data using IMOD. J. Struct. Biol. *116*, 71–76.

Kwiatkowski da Silva, A., Ponge, D., Peng, Z., Inden, G., Lu, Y., Breen, A., Gault, B., and Raabe, D. (2018). Phase nucleation through confined spinodal fluctuations at crystal defects evidenced in Fe-Mn alloys. Nat. Commun. *9*, 1137.

Lee, D., Huh, J.-Y., Jeong, D., Shin, J., Yun, A., and Kim, J. (2014). Physical, mathematical, and numerical derivations of the Cahn–Hilliard equation. Comput Mater. Sci. *81*, 216–225.

Lee, T.C., Kashyap, R.L., and Chu, C.N. (1994). Building skeleton models via 3-D medial surface axis thinning algorithms. CVGIP: Graph. Models Image Process. *56*, 462–478.

Lei, D., Marras, A.E., Liu, J., Huang, C.M., Zhou, L., Castro, C.E., Su, H.J., and Ren, G. (2018). Three-dimensional structural dynamics of DNA origami Bennett linkages using individual-particle electron tomography. Nat. Commun. *9*, 592.

Loh, N.D., Sen, S., Bosman, M., Tan, S.F., Zhong, J., Nijhuis, C.A., Král, P., Matsudaira, P., and Mirsaidov, U. (2017a). Multistep nucleation of nanocrystals in aqueous solution. Nat. Chem. *9*, 77–82.

Luger, K., Mäder, A.W., Richmond, R.K., Sargent, D.F., and Richmond, T.J. (1997). Crystal structure of the nucleosome core particle at 2.8 A resolution. Nature *389*, 251–260.

Maeshima, K., Imai, R., Hikima, T., and Joti, Y. (2014a). Chromatin structure revealed by X-ray scattering analysis and computational modeling. Methods *70*, 154–161.

Maeshima, K., Imai, R., Tamura, S., and Nozaki, T. (2014b). Chromatin as dynamic 10-nm fibers. Chromosoma *123*, 225–237.

Maeshima, K., Rogge, R., Tamura, S., Joti, Y., Hikima, T., Szerlong, H., Krause, C., Herman, J., Seidel, E., DeLuca, J., et al. (2016). Nucleosomal arrays selfassemble into supramolecular globular structures lacking 30-nm fibers. EMBO J. *35*, 1115–1132.

Narayan, K., and Subramaniam, S. (2015). Focused ion beams in biology. Nat. Methods *12*, 1021–1031.

Nishino, Y., Eltsov, M., Joti, Y., Ito, K., Takata, H., Takahashi, Y., Hihara, S., Frangakis, A.S., Imamoto, N., Ishikawa, T., and Maeshima, K. (2012). Human mitotic chromosomes consist predominantly of irregularly folded nucleosome fibres without a 30-nm chromatin structure. EMBO J. *31*, 1644–1653.

Ostwald, W. (1897). Studies on the formation and transformation of solid bodies. Z. Phys. chem. *22*, 289–330.

Ou, H.D., Phan, S., Deerinck, T.J., Thor, A., Ellisman, M.H., and O'Shea, C.C. (2017). ChromEMT: visualizing 3D chromatin structure and compaction in interphase and mitotic cells. Science *357*.

Palikyras, S., and Papantonis, A. (2019). Modes of phase separation affecting chromatin regulation. Open Biol. *9*, 190167.

Pearson, K. (1901). On lines and planes of closest fit to systems of points in space. Lond. Edinb. Dublin Philos. Mag. J. Sci. *2*, 559–572.

Pettersen, E.F., Goddard, T.D., Huang, C.C., Couch, G.S., Greenblatt, D.M., Meng, E.C., and Ferrin, T.E. (2004). UCSF Chimera–a visualization system for exploratory research and analysis. J. Comput. Chem. *25*, 1605–1612.

Pong, B.-K., Elim, H.I., Chong, J.-X., Ji, W., Trout, B.L., and Lee, J.-Y. (2007). New insights on the nanoparticle growth mechanism in the citrate reduction of gold (III) salt: formation of the Au nanowire intermediate and its nonlinear optical properties. J. Phys. Chem. C *111*, 6281–6287.

Rames, M., Yu, Y.D., and Ren, G. (2014). Optimized negative staining: a high-throughput protocol for examining small and asymmetric protein structure by electron microscopy. J. Vis. Exp. e51087.

Razin, S.V., and Gavrilov, A.A. (2014). Chromatin without the 30-nm fiber: constrained disorder instead of hierarchical folding. Epigenetics *9*, 653–657.

Molecular Cell
Article

CellPress
OPEN ACCESS

Robinson, P.J., Fairall, L., Huynh, V.A., and Rhodes, D. (2006). EM measurements define the dimensions of the "30-nm" chromatin fiber: evidence for a compact, interdigitated structure. Proc. Natl. Acad. Sci. USA *103*, 6506–6511.

Robinson, P.J., and Rhodes, D. (2006). Structure of the '30 nm' chromatin fibre: a key role for the linker histone. Curr. Opin. Struct. Biol. *16*, 336–343.

Sanulli, S., and J Narlikar, G. (2020). Liquid-like interactions in heterochromatin: implications for mechanism and regulation. Curr. Opin. Cell Biol. *64*, 90–96.

Sanulli, S., Trnka, M.J., Dharmarajan, V., Tibble, R.W., Pascal, B.D., Burlingame, A.L., Griffin, P.R., Gross, J.D., and Narlikar, G.J. (2019). HP1 reshapes nucleosome core to promote phase separation of heterochromatin. Nature *575*, 390–394.

Schalch, T., Duda, S., Sargent, D.F., and Richmond, T.J. (2005). X-ray structure of a tetranucleosome and its implications for the chromatin fibre. Nature *436*, 138–141.

Scheffer, M.P., Eltsov, M., and Frangakis, A.S. (2011). Evidence for short-range helical order in the 30-nm chromatin fibers of erythrocyte nuclei. Proc. Natl. Acad. Sci. USA *108*, 16992–16997.

Schmelzer, J.W., Abyzov, A.S., and Möller, J. (2004). Nucleation versus spinodal decomposition in phase formation processes in multicomponent solutions. J. Chem. Phys. *121*, 6900–6917.

Schorb, M., Haberbosch, I., Hagen, W.J.H., Schwab, Y., and Mastronarde, D.N. (2019). Software tools for automated transmission electron microscopy. Nat. Methods *16*, 471–477.

Sear, R.P. (2014). Quantitative studies of crystal nucleation at constant supersaturation: experimental data and models. CrystEngComm *16*, 6506–6522.

Shakya, A., Park, S., Rana, N., and King, J.T. (2020). Liquid-liquid phase separation of histone proteins in cells: role in chromatin organization. Biophys. J. *118*, 753–764.

Shin, Y., and Brangwynne, C.P. (2017). Liquid phase condensation in cell physiology and disease. Science *357*, eaaf4382.

Shin, Y., Chang, Y.C., Lee, D.S.W., Berry, J., Sanders, D.W., Ronceray, P., Wingreen, N.S., Haataja, M., and Brangwynne, C.P. (2018). Liquid nuclear condensates mechanically sense and restructure the genome. Cell *175*, 1481–1491.e13.

Song, F., Chen, P., Sun, D., Wang, M., Dong, L., Liang, D., Xu, R.M., Zhu, P., and Li, G. (2014). Cryo-EM study of the chromatin fiber reveals a double helix twisted by tetranucleosomal units. Science *344*, 376–380.

Strohkendl, I., Saifuddin, F.A., Gibson, B.A., Rosen, M.K., Russell, R., and Finkelstein, I.J. (2021). Inhibition of CRISPR-Cas12a DNA targeting by nucleosomes and chromatin. Sci. Adv. *7*, eabd6030.

Strom, A.R., Emelyanov, A.V., Mir, M., Fyodorov, D.V., Darzacq, X., and Karpen, G.H. (2017). Phase separation drives heterochromatin domain formation. Nature *547*, 241–245.

Tang, G., Peng, L., Baldwin, P.R., Mann, D.S., Jiang, W., Rees, I., and Ludtke, S.J. (2007). EMAN2: an extensible image processing suite for electron microscopy. J. Struct. Biol. *157*, 38–46.

Thanh, N.T., Maclean, N., and Mahiddine, S. (2014). Mechanisms of nucleation and growth of nanoparticles in solution. Chem. Rev. *114*, 7610–7630.

Ulianov, S.V., Velichko, A.K., Magnitov, M.D., Luzhin, A.V., Golov, A.K., Ovsyannikova, N., Kireev, I.I., Gavrikov, A.S., Mishin, A.S., Garaev, A.K., et al. (2021). Suppression of liquid-liquid phase separation by 1,6-hexanediol partially compromises the 3D genome organization in living cells. Nucleic Acids Res. *49*, 10524–10541.

Vekilov, P.G. (2010). The two-step mechanism of nucleation of crystals in solution. Nanoscale *2*, 2346–2357.

Weigert, M., Schmidt, U., Boothe, T., Müller, A., Dibrov, A., Jain, A., Wilhelm, B., Schmidt, D., Broaddus, C., Culley, S., et al. (2018). Content-aware image restoration: pushing the limits of fluorescence microscopy. Nat. Methods *15*, 1090–1097.

Widom, J., and Klug, A. (1985). Structure of the 300A chromatin filament: X-ray diffraction from oriented samples. Cell *43*, 207–213.

Wittmeyer, J., Saha, A., and Cairns, B. (2004). DNA translocation and nucleosome remodeling assays by the RSC chromatin remodeling complex. Methods Enzymol. *377*, 322–343.

Wright, R.H.G., Le Dily, F., and Beato, M. (2019). ATP, Mg^{2+}, nuclear phase separation, and genome accessibility. Trends Biochem. Sci. *44*, 565–574.

Yau, S.T., and Vekilov, P.G. (2001). Direct observation of nucleus structure and nucleation pathways in apoferritin crystallization. J. Am. Chem. Soc. *123*, 1080–1089.

Zhai, X., Lei, D., Zhang, M., Liu, J., Wu, H., Yu, Y., Zhang, L., and Ren, G. (2020). LoTToR: an algorithm for missing-wedge correction of the low-tilt tomographic 3D reconstruction of a single-molecule structure. Sci. Rep. *10*, 10489.

Zhang, K. (2016). Gctf: real-time CTF determination and correction. J. Struct. Biol. *193*, 1–12.

Zhang, L., Lei, D., Smith, J.M., Zhang, M., Tong, H., Zhang, X., Lu, Z., Liu, J., Alivisatos, A.P., and Ren, G. (2016). Three-dimensional structural dynamics and fluctuations of DNA-nanogold conjugates by individual-particle electron tomography. Nat. Commun. *7*, 11083.

Zhang, L., and Ren, G. (2012). IPET and FETR: experimental approach for studying molecular structure dynamics by cryo-electron tomography of a single-molecule structure. PLoS One *7*, e30249.

Zhang, Y., and Kutateladze, T.G. (2019). Liquid–liquid phase separation is an intrinsic physicochemical property of chromatin. Nat. Struct. Mol. Biol. *26*, 1085–1086.

Zheng, S.Q., Palovcak, E., Armache, J.P., Verba, K.A., Cheng, Y., and Agard, D.A. (2017). MotionCor2: anisotropic correction of beam-induced motion for improved cryo-electron microscopy. Nat. Methods *14*, 331–332.

Zhou, B.R., Feng, H., Ghirlando, R., Li, S., Schwieters, C.D., and Bai, Y. (2016). A small number of residues can determine if linker histones are bound on or off dyad in the chromatosome. J. Mol. Biol. *428*, 3948–3959.

Zhou, C.Y., and Narlikar, G.J. (2016). Analysis of nucleosome sliding by ATP-dependent chromatin remodeling enzymes. Methods Enzymol. *573*, 119–135.

STAR★METHODS

KEY RESOURCES TABLE

REAGENT or RESOURCE	SOURCE	IDENTIFIER
Bacterial strains		
dam-/dcm- Competent E. coli	New England Biolabs	C2925I
DH5α E. coli competent cells	Macrolab, QB3-Berkeley	N/A
BL21(DE3) pLysS E. coli competent cells	Macrolab, QB3-Berkeley	N/A
Chemicals, Peptides, and Recombinant Proteins		
Cyanine3 maleimide	Lumiprobe	21080
TCEP (Tris(2-carboxyethyl) phosphine hydrochloride)	Sigma-Aldrich	C4706
E. coli DNA Ligase	New England Biolabs	M0205
T4 DNA Ligase	New England Biolabs	M0202
BbsI-HF	New England Biolabs	R3539
BsaI-HFv2	New England Biolabs	R3733
Glucose Oxidase	Sigma-Aldrich	G2133
Catalase	Sigma-Aldrich	C9322
Human H1.0 linker histone	The Histone Source, Colorado State University	N/A
EDTA-free Protease Inhibitor Cocktail	Roche	04693159001
mPEG-Succinimidyl Valerate, MW 5,000	Laysan Bio	MPEG-SVA-5000
Gel Loading Dye, Purple with SDS	New England Biolabs	B7024
Xenopus H2A K119C	The Histone Source, Colorado State University	XH2A_K119C
Deposited Data		
Early irregular condensate, 1	This paper	EMD-24888
Early irregular condensate, 2	This paper	EMD-24901
Early irregular condensate, 3	This paper	EMD-24902
Early irregular condensate, 4	This paper	EMD-24903
Intermediate irregular condensate,1	This paper	EMD-24914
Intermediate irregular condensate, 2	This paper	EMD-24915
Intermediate irregular condensate, 3	This paper	EMD-24916
Intermediate irregular condensate, 4	This paper	EMD-24917
Late irregular condensate, 1	This paper	EMD-24918
Late irregular condensate, 2	This paper	EMD-24919
Late irregular condensate, 3	This paper	EMD-24920
Late irregular condensate, 4	This paper	EMD-24921
Small spherical condensate, 1	This paper	EMD-24923
Small spherical condensate, 2	This paper	EMD-24924
Small spherical condensate, 3	This paper	EMD-24925
Small spherical condensate, 4	This paper	EMD-24926
Gown spherical condensate, 1	This paper	EMD-24904
Gown spherical condensate, 2	This paper	EMD-24905
Gown spherical condensate, 3	This paper	EMD-24906
Gown spherical condensate, 4	This paper	EMD-24907
Gown spherical condensate, 5	This paper	EMD-24908
Gown spherical condensate with H1, 1	This paper	EMD-24909
Gown spherical condensate with H1, 2	This paper	EMD-24910

Molecular Cell
Article

CellPress
OPEN ACCESS

Continued

REAGENT or RESOURCE	SOURCE	IDENTIFIER
Gown spherical condensate with H1, 3	This paper	EMD-24911
Gown spherical condensate with H1, 4	This paper	EMD-24912
Gown spherical condensate with H1, 5	This paper	EMD-24913
Oligonucleotides		
Forward primer for 100 bp 1st nucleosome of tetranucleosome DNA template: 5' ATTCCAG TTGGTCTCTCAACAGCTTGCATGCCTGCAGGTCC 3'	IDT	N/A
Forward primer for 70 bp 1st nucleosome of tetranucleosome DNA template:5' ATTCCAGTTGGTCTCTCAACATGAC CAAGGAAAGCATGATTC 3'	IDT	N/A
Reverse primer for 1st nucleosome of tetranucleosome DNA template: 5' AGTTGTACTGTAGTCTTCCAATACAT GCACAGGATGTATATATCTG 3'	IDT	N/A
Forward primer for 2nd nucleosome of tetranucleosome DNA template: 5' ATTCCAGTTGAAGACTACAGTACCCT ATACGCGGCCGCCCTGGAGAAT 3'	IDT	N/A
Reverse primer for 2nd nucleosome of tetranucleosome DNA template: 5' AGTTGTGTCATAGTCTTCCAATACATG CACAGGATGTATATATCTG 3'	IDT	N/A
Forward primer for 3rd nucleosome of tetranucleosome DNA template: 5' ATTCCAGTTGAAGACTATGACACCCT ATACGCGGCCGCCCTGGAGAAT 3'	IDT	N/A
Reverse primer for 3rd nucleosome of tetranucleosome DNA template: 5' AGTTGTTGCGTAGTCTTCCAATACAT GCACAGGATGTATATATCTG 3'	IDT	N/A
Forward primer for 4th nucleosome of tetranucleosome DNA template: 5' ATTCCAGTTGAAGACTACGCAACCC TATACGCGGCCGCCCTGGAGAAT 3'	IDT	N/A
Reverse primer for 4th nucleosome of tetranucleosome DNA template: 5' AACTGGAATGGTCTCAAGGACTCGG AACACTATCCGACTGGCAC 3'	IDT	N/A
Forward primer for 30 bp 5' biotin ds oligo: 5' /5Biosg/ TCTTCACACCGAGTTCATCCCTTATG 3'	IDT	N/A
Reverse primer for 30 bp 5' biotin ds oligo: 5' GTTGCAT AAGGGATGAACTCGGTGTGAAGA 3'	IDT	N/A
Recombinant DNA		
Plasmid: pGEM-3Z/601	Addgene	26656
pGEM-3Z/601_4x601_40bplinker	This paper	N/A
Plasmid: Pet3a_H2A (Xenopus laevis)	Narlikar Lab	N/A
Plasmid: Pet3a_H2B (Xenopus laevis)	Narlikar Lab	N/A
Plasmid: Pet3a_H23 (Xenopus laevis)	Narlikar Lab	N/A
Plasmid: Pet3a_H4 (Xenopus laevis)	Narlikar Lab	N/A
Software and Algorithms		
IMOD	(Kremer et al., 1996)	https://bio3d.colorado.edu/imod/
Serial EM	(Schorb et al., 2019)	https://bio3d.colorado.edu/SerialEM/
MotionCor2	(Zheng et al., 2017)	https://msg.ucsf.edu/software
GCTF	(Zhang, 2016)	https://www2.mrc-lmb.cam.ac.uk/research/locally-developed-software/zhang-software/

(Continued on next page)

CellPress
OPEN ACCESS

Molecular Cell
Article

Continued

REAGENT or RESOURCE	SOURCE	IDENTIFIER
UCSF Chimera	(Pettersen et al., 2004)	https://www.cgl.ucsf.edu/chimera/
EMAN2	(Tang et al., 2007)	https://blake.bcm.edu/emanwiki/EMAN2
CARE	(Weigert et al., 2018)	https://csbdeep.bioimagecomputing.com/tools/care/
TomoCTF	(Fernández et al., 2006)	https://sites.google.com/site/3demimageprocessing/tomoctf
DBSCAN	(Ester et al., 1996)	https://scikit-learn.org/stable/modules/generated/sklearn.cluster.DBSCAN.html
3D skeletonizing	(Lee et al., 1994)	https://scikit-image.org/docs/0.13.x/auto_examples/edges/plot_skeleton.html
IPET	(Zhang and Ren, 2012)	Available on request
LoTToR	(Zhai et al., 2020)	Available on request
Other		
Biotinyl Cap PE	Avanti	870277
streptavidin	New England Biolabs	N7021S
Superdex 200 Increase 10/300 GL	Cytiva	28990944
Model 491 Prep Cell	Bio-Rad	1702928
Density Gradient Fractionation System	Brandel	BR-186
QUANTIFOIL S7/2 300 mesh Au carbon grids	ELECTRON MICROSCOPY SCIENCES	https://www.emsdiasum.com/
Lacey LC-Au-FF 200 mesh Au carbon grids	ELECTRON MICROSCOPY SCIENCES	https://www.emsdiasum.com/

RESOURCE AVAILABILITY

Lead contact
Further information and requests for resources and reagents should be directed to and will be fulfilled by the lead contact, Carlos Bustamante (carlosjbustamante2@gmail.com).

Materials availability
All unique reagents generated in this study are available from the lead contact with a completed Materials Transfer Agreement.

Data code and availability
- The denoised final maps generated in this study is available on the Electron Microscopy Data Bank (EMDB) with the accession number EMD-24XXX, as listed in the key resources table.
- The code to reproduce statistics and figures has been deposited at GitHub Zenodo (https://doi.org/10.5281/zenodo.6579000).
- Any additional information required to reanalyze the data reported in this paper is available from the lead contact upon request.

METHOD DETAILS

Purification of histones proteins
Purification of *Xenopus laevis* histones H2A, H2B, H3, and H4, was performed as previously described (Wittmeyer et al., 2004). Briefly, histone plasmids were transformed into *E. coli* BL21(DE3) and bacterial cells were grown at 37°C in LB media supplemented with ampicillin and chloramphenicol. Histone expression was induced at an OD_{600} of ~0.6 by adding Isopropyl β-D-1-thiogalactopyranoside (IPTG) at a final concentration of 1 mM. After 3 h of induction, cell cultures were pelleted, suspended in wash buffer (50 mM Tris-HCl pH 7.5; 100 mM NaCl; 1 mM EDTA; 5 mM 2-mercaptoethanol (BME); 1% Triton X-100 [w/v]; and protease inhibitors (Roche)) and frozen at -80°C for later use. To purify the inclusion bodies, cell pellets were thawed, sonicated, and centrifuged at 25,000 x g for 30 min. The resulting pellet was rinsed, suspended in wash buffer, and centrifuged three times. The detergent was

Molecular Cell
Article

removed by rinsing and centrifugating (three times) the inclusion bodies with wash buffer without Triton X-100. Inclusion bodies were then solubilized in 20 mM Tris-HCl pH 7.5; 8 M Urea; 1 mM EDTA; 10 mM DTT, and purified by anion and cation exchange. Purification was checked by 15% SDS-PAGE, fractions containing pure histones were pooled and dialyzed against 1 L of 10 mM Tris pH 8.0. Histones were centrifuged to remove aggregates, concentrated (~10 mg/mL), lyophilized, and stored at -80°C.

Fluorescence labeling of H2A
For fluorescence microscopy experiments, *Xenopus laevis* histone H2A119C (The Histone source, Colorado State University) was chemically modified with the fluorescent dye Cy3 (Cyanine3 maleimide; Lumiprobe) diluted in dimethylformamide (DMF) as previously shown, with some modifications (Zhou and Narlikar, 2016). Lyophilized H2A119C was resuspended to 2 mg/mL using labeling buffer (20 mM Tris-HCL, pH 7.0; 7 M guanidine hydrochloride; 5 mM EDTA) and incubated for 2 h at room temperature. Unfolded histone was first reduced with 100 mM TCEP (Sigma) for 2 h in the dark, followed by a second round at the same concentration but overnight. H2A119C was labeled by adding 15-fold molar excess of Cy3 maleimide (~2 mM) at 21°C overnight, in the dark and constant shaking. The non-conjugated Cy3 maleimide was removed by centrifugation using a Microcon of 3.5 kDa membrane cutoff. Concentrated Cy3-histone was diluted with labeling buffer and concentrated again. This procedure was repeated six times, and every other time, the Microcon filter was changed for a new one. Concentration of labeled histone and degree of Cy3 labeling was ~50%, which was calculated by measuring the absorbance at 278 nm and 555 nm and using the extinction coefficients of 4,400 Mcm^{-1} and 150,000Mcm^{-1} for H2A119C and Cy3, respectively.

Histone octamer reconstitution
To reconstitute the wild type histone octamer (Wittmeyer et al., 2004) and the Cy3-labeled octamer (H2A-Cy3 replaces H2A), lyophilized histones were solubilized with unfolding buffer (20 mM Tris-HCl pH 7.5; 7 M guanidine hydrochloride; 10 mM DTT), combined at a H2A:H2B:H3:H4 ratio of 1.2:1.2:1:1, and dialyzed 4 times against 1 L of refolding buffer (10 mM Tris-HCl pH 8.0; 2 M NaCl; 1 mM EDTA; 5 mM DTT), with three buffer exchanges, for a total of 48 h. Refolded octamer was centrifuged, concentrated to ~0.5 mL, and loaded onto Superdex 200 Increase 10/300 GL (Cytiva) equilibrated with refolding buffer. Gel filtration separated octamers from aggregates, tetramers, and dimers. Fractions were checked by 15% SDS-PAGE, and fractions containing the four histones in equimolar quantities (based on Coomassie blue staining) were pooled, concentrated to ~10 mg/mL, and stored at -80°C. Fractions containing H2A-H2B heterodimer were also pooled, concentrated to ~10 mg/mL, and stored at -80°C.

Synthesis of tetranucleosome and dodecamer array DNA templates
The tetranucleosome DNA template array contains four repeats of the 601-nucleosome positioning sequence separated by a 40 bp linker length, and flanked to the left by 100 bp DNA, and to the right by 50 bp DNA (100-4W-50; left and right sides correspond to the 5' and 3' ends, using the 601 sequence (W) as a reference). Tetranucleosome DNA template was synthetized by ligation of four fragments containing one 601 sequence each. Each fragment was produced by PCR using the pGEM-3Z/601 plasmid (Addgene), which contains the 601 nucleosome positioning sequence. Primers containing the restriction recognition sites for enzymes BbsI and BsaI (NEB) were used to amplify the 601 sequence. BbsI and BsaI recognizes asymmetric DNA sequences and cut outside of their recognition sequence, allowing the ligation in tandem of DNA fragments, and the control over the number of repeats. In our design, the tetranucleosome is flanked by two BsaI sites, and the BbsI sites were used to ligate the four nucleosome fragments. In the first cleavage step, the four fragments were digested with BbsI and ligated at an equimolar ratio using *E. coli* DNA ligase (NEB). The longest product, corresponding to the tetranucleosome, was purified from 0.8% agarose gels, digested using the BsaI enzyme, and cloned into BsaI-restricted pGEM-3Z/601 plasmid using T4 DNA ligase (NEB). Ligation product was transformed into *E. coli* DH5α for plasmid extraction by miniprep. The product of the tetranucleosome DNA synthesis was checked by DNA sequencing. The dodecamer nucleosome array was synthetized by ligation of three tetranucleosome templates. Resulting ligation product was digested using BsaI enzyme and cloned into BsaI-restricted pGEM-3Z/601.

To produce large quantities of the tetranucleosome DNA template, the tetranucleosome plasmid was grown in *dam⁻/dcm⁻ E. coli* cells (NEB), and it was purified by maxiprep. Tetranucleosome DNA template was excised from the vector backbone by digestion using the BsaI enzyme. Tetranucleosome template was purified by preparative 5% acrylamide electrophoresis using the Model 491 Prep Cell (Bio-Rad) electroelution system. The dodecamer array was produced and purified in the same way as tetranucleosome DNA template, but using preparative 4% acrylamide electrophoresis.

Synthesis of biotinylated tetranucleosome and dodecamer arrays
To incorporate a biotin molecule to the 100-4W-50 template without modifying its length, a 70-4W-50 template was ligated with a biotinylated 30 bp dsDNA to produce the biotin-100-4W-50 DNA template. The 70-4W-50 template was designed and produced in the same way as the 100-4W-50. The 30 bp dsDNA was synthesized by the annealing of two complementary oligos (IDT), forming a 5' biotinylated end and a 3' end with a BsaI overhang, which is complementary to the left side of 70-4W-50. Biotin-30 bp ds oligo and 70-4W-50 were ligated using T4 ligase at a molar ratio of 20:1, respectively. Ligation reaction was inactivated with SDS loading buffer (NEB), and the biotin-100-4W-50 product was purified by preparative 5% acrylamide electrophoresis using the Model 491 Prep Cell system.

In vitro reconstitution of tetranucleosome and dodecamer arrays

Wild type histone octamers and tetranucleosome DNA templates (100-4W-50 and biotin-100-4W-50) were combined at a ratio of 1:1.2, respectively, in 200 μL of high-salt buffer (10 mM Tris-Cl pH 8.0; 2 M NaCl; 1 mM EDTA; 0.5 mM DTT; and 1 mM PMSF) at a final concentration of 100 ng/uL of DNA template. H2A-H2B dimer was also incorporated at a molar ratio of 0.2 compared to the octamer to promote nucleosome, rather than hexasome formation. For fluorescent nucleosome arrays, wild type octamers were doped with 25% Cy3-octamer and combined with the 100-4W-50 template. Tetranucleosome assembly solutions were dialyzed against 500 mL of high-salt buffer for 1 h at 4°C, followed by a lineal gradient dialysis against 2 L of low-salt buffer (10 mM Tris-Cl pH 8.0; 1 mM EDTA; 0.5 mM DTT; and 1 mM PMSF) using a peristaltic pump at 0.8 mL/min and with continued stirring. A final dialysis of 3 h in 500 mL of low salt buffer was done to reduce the residual NaCl concentration, and the nucleosome reconstitution was checked by 4% acrylamide native electrophoresis.

Reconstituted arrays were loaded into 4.8 mL of 10-40% lineal sucrose gradient (20 mM HEPES-NaOH pH 7.5; 1 mM EDTA; 1 mM DTT) and centrifuged for 16 h at 38,000 rpm at 4°C, using an ultracentrifuge Beckman Optima MAX-XP with the rotor MLS-50 (Beckmann). Gradients were fractionated into 100 μL fractions using a gradient fractionator (Brandel), and the resulting purification was checked by 4% acrylamide native electrophoresis. Fractions containing 1-2 bands were pooled, concentrated, dialyzed against 20 mM HEPES-NaOH pH 7.5; 1 mM EDTA; and 1 mM DTT, and stored at 4°C. Tetranucleosome purification was checked by atomic force microscopy (AFM). The dodecamer arrays were synthetized and purified in the same way as tetranucleosomes, but the loading was verified by 0.8% TBE agarose gel and atomic force microscopy (AFM).

Atomic force microscopy of nucleosome arrays

Purified tetranucleosome and dodecamer arrays were diluted to 10 nM and crosslinked with 1% formaldehyde for 1 h at room temperature. Crosslinked sample was dialyzed against 20 mM HEPES-NaOH pH 7.5; 1 mM EDTA; 1 mM DTT, and centrifuged at 20,000 x g to remove aggregates. Crosslinked nucleosome array samples were diluted to 1 nM using 10 mM MOPS pH 7.0 and 5 mM MgCl$_2$, and 3 μL of sample were deposited and incubated for 2 min on freshly cleaved bare mica V1 (Ted Pella Inc.), after which was rinsed with Milli-Q water, and then gently dried under a stream of N2 perpendicular to the mica surface. AFM micrographs were taken with a MultiMode NanoScope 8 atomic force microscope (Bruker Co.) equipped with a vertical engagement scanner E. The samples were excited at their resonance frequency (280-350 kHz) with free amplitudes (Ao) of 2-10 nm and imaged in tapping mode using silicon cantilevers (Nanosensors). The image amplitude (set point As) and A0 ratio (As/A0) was kept at ~0.8 in a repulsive tip-sample interaction regime, and phase oscillations were no greater than ± 5 degrees. The surface was rastered following the fast scan axis (x) at rates of 2 Hz, capturing the retrace line to reconstruct the AFM micrographs. All samples were scanned at room temperature in air, at a relative humidity of 30%.

Tetranucleosome phase transition visualized by epifluorescence microscopy

For phase transition experiments using fluorescence microscopy, tetranucleosome stocks 100-4W-50 (300 nM) and Cy3-100-4W-50 (300 nM) were combined at a molar ratio of 3:1, respectively, in 10 mM HEPES-NaOH pH 7.5; 1 mM EDTA; and 1 mM DTT. Nucleosome phase transition was induced by diluting the tetranucleosome stocks tenfold in 50 mM Tris-HCl pH 7.5; 150 mM NaCl; 5 mM MgCl$_2$; and 1 mM DTT. Phase transition reactions were incubated at room temperature, and 4.5 μL aliquots were combined at different times with 0.5 μL of 10X GODCAT visualization buffer (50 mM Tris-HCl pH 7.5; 2 mg/mL Glucose Oxidase (SIGMA cat. no. G2133); 350 ng/mL Catalase (SIGMA cat. no. C1345); 20% Glucose; 10 mg/mL AcBSA (Thermo); 50% glycerol) and added into the PEGylated and BSA passivated slide/coverslip chamber.

To prepare the visualization chamber, glass coverslips and slides were passivated using polyethylene glycol (PEG) as previously described (Chandradoss et al., 2014). A microfluidic chamber was assembled with both the PEG-coverslip and the PEG-slide, and the channel formed between both surfaces was blocked for 30 min by the addition of 1 mg/mL of AcBSA (Thermo) in 20 mM Tris-HCl pH 7.5; 50 mM NaCl, and 1 mM EDTA, followed by rinsing with 50 mM Tris-Cl pH 7.5; 150 mM NaCl; 5 mM MgCl$_2$; and 1 mM DTT. 5 μL of the phase transition reaction combined with the GODCAT was applied to the channel chamber and visualized using epifluorescence microscopy. Nucleosome phase transition in the presence of human H1.0 linker histone (The Histone Source, Colorado State University) was performed in the same way as explained above, but including H1 in the phase transition reaction at a concentration of 120 nM to keep a ratio of H1: nucleosome 1:1.

Epifluorescence micrographs were taken using a laboratory built wide-field fluorescence microscope. An oil-immersion 100x objective lens (Olympus 100× UPlansApo, N.A. 1.4) was used with a diode-pumped 532-nm laser (75 mW; CrystaLaser) for excitation and a red LED for brightfield illumination. Fluorescence emissions and brightfield illumination were splitted via a laboratory-built multi-channel imaging system and projected side-by-side on an EMCCD (IXon EM+ 897; Andor). The illuminated area on each channel was ~50 × 25 μm with ~110 nm pixel widths.

Fluorescence recovery after photobleaching (FRAP) of tetranucleosomes

FRAP was performed on 300 nM H2A-Cy3 tetranucleosome droplets using a Nikon TIRF inverted scope (Nikon Eclipse Ti2, 488/560/642nm OPSL lasers) with perfect focus, a 100x N.A. 1.4 APO TIRF oil objective, Nikon TIRF/iLAS2 FRAP Module (Gataca Systems) and an EMCCD camera (Photometrics Prime 95B). The droplets were imaged every 5 s for 15 s of pre-bleach, and every 5 s for 250 s

Molecular Cell
Article

CellPress
OPEN ACCESS

after photobleaching. Photobleaching was performed with a 561 nm laser (100% laser power; 50 μs irradiation). FRAP data was processed by the normalization method. The first-post bleach point was set to zero.

Nucleosome array phase transition visualized by OpNS-EM

Tetranucleosome stocks 100-4W-50 and biotin-100-4W-50 were combined at a molar ratio of 3:1, respectively, in 20 mM HEPES-NaOH pH 7.5; 1 mM EDTA; and 1 mM DTT. Nucleosome phase transition was induced by diluting tenfold the tetranucleosome stocks in buffers with different salt concentrations (20 mM HEPES-NaOH pH 7.5; 0-150 mM NaCl; 0-5 mM MgCl$_2$; and 1 mM DTT) at a final tetranucleosome concentration of 30 nM (This value has been used for all of the following incubation experiments. And to keep the total nucleosome concentration consistent, the dodecamer arrays were diluted to 10 nM during incubation). Phase transition reactions were incubated at 4°C, 20°C, and 36°C, and were analyzed at different incubation times by the optimized negative staining protocol (OpNS) as previously described (Rames et al., 2014). In brief, 4 μL of the phase transition reaction was deposited on a glow-discharged ultra-thin carbon-coated 200-mesh copper grid (CF200-Cu-UL, Electron Microscopy Sciences, Hatfield, PA, USA, and Cu-200CN, Pacific Grid-Tech, San Francisco, CA, USA). After 30 seconds of incubation, phase transition solution on the grid was blotted with filter paper. The grid was stained for 10 s with 30 μL of 1% (w/v) uranyl formate (UF), UF was blotted with filter paper, and the staining procedure was repeated two more times, followed by air-drying with nitrogen. OpNS images were acquired under a defocus of 0.5-1 μm on a Zeiss Libra 120 Plus transmission electron microscope (TEM) (Carl Zeiss NTS GmbH) equipped with a Gatan UltraScan 4 k × 4 k CCD. The TEM was set to a high-tension of 120 kV with energy filtering at 20 eV. Carbon-coated grids are usually glow-discharged in residual air to promote the absorption of biological material deposition from the aqueous solution, a process that makes the surface hydrophilic by depositing negative charges. However, the negatively charged surface does not efficiently bind the negatively charged nucleosome arrays at low ionic strength (due to weak shielding effect, see Figure S3D; blue section). An analysis of the effect of Na$^+$ and Mg^{2+} within a 10 min incubation interval indicated that in absence of Na$^+$, spherical condensates were formed above 0.5 mM Mg^{2+}, but irregular condensates were not observed (Figure S3D, left column). When tetranucleosomes were incubated in absence of Mg^{2+}, tetranucleosomes formed irregular condensates above 1.5 mM Na$^+$ (Figure S3D, middle column). When Mg^{2+} and Na$^+$ are both present, high concentration of Na$^+$ caused a delayed formation of SphCs (Figure S3D, right column).

Preparation of streptavidin 2D crystal grids and cryo-EM sample deposition

The streptavidin (SA) crystal grids were prepared as previously described (Han et al., 2016) with a few modifications. Lacey carbon grids with 5 μm holes (LC200-Au-FF, Electron Microscopy Sciences) and Quantifoil carbon grids with 7 μm holes (S 7/2, Electron Microscopy Sciences) were cleaned with 100% chloroform to remove the plastic cover. Since functionalization of carbon grids involves hydrophobic interactions, no glow discharge was applied on the grids. To form a biotinylated monolayer of lipids, 30 μL of castor oil (BRAND) was added to 5 ml of crystallization buffer (50 mM HEPES-NaOH pH 7.5; 150 mM KCl; and 5 mM EDTA) in a 50 mm plastic petri dish, followed by the addition of 1 μL of 1 mg/mL Biotinyl Cap PE (1,2-dipalmitoyl-sn-glycero-3-phosphoethanol-amine-N-(cap biotinyl); Avanti). To functionalize the grids, cleaned carbon grids were put in contact with the lipid monolayer for 1 s, then washed three times with 100 μL of crystallization buffer. To add the streptavidin surface to the grid, 4 μL of 0.2 mg/mL of streptavidin (NEB) in crystallization buffer were added to the biotinylated lipid surface and incubated for 30 min in a humidity chamber at room temperature. To remove excess of SA, SA-crystal grids were washed and blocked with 30 μl of rinsing buffer (10 mM HEPES-NaOH pH 7.5; 50 mM KCl; 5 mM EDTA; and 10% trehalose) followed by blotting and air drying. A thin layer of carbon was deposited by evaporation onto the backside of the SA crystal grid to protect the crystal from being damaged during grid manipulation. SA-crystal grids were stored at room temperature in a sealed box for further use.

For sample deposition, excess trehalose was removed from SA crystal grids by rinsing the grids two times with 30 μL of crystallization buffer for 10 min. Grids were blotted at the edge with filter paper, then 4 μL of the tetranucleosome phase transition reactions (prepared as for OpNS-EM visualization) were added to the SA grids and incubated in a humidity chamber to allow for biotin and streptavidin binding. After 2 min, grids were blotted for 2 s and immediately flash frozen in liquid ethane at 100% humidity to form an amorphous ice, using a Leica EM GP rapid-plunging device (Leica, Buffalo Grove, IL, USA). Humidity chamber and the plunging device were set to the temperature used in each phase transition reaction.

Cryo-ET data acquisition

We found that the negatively charged nucleosome arrays did not efficiently bind to the negatively charged carbon grids. An increased ionic strength not only facilitates the nucleosome grid surface deposition, but also affect the nucleosome condensates formation (Figure S3D). To avoid using a charged grid surface, we used the 2D streptavidin crystal grid (Han et al., 2016) and tetranucleosome arrays harboring a biotin molecule at one DNA end for sample deposition. The similar appearance of large condensates on grids prepared with and without the streptavidin crystal, after long incubation times indicated that the condensates form in solution and are then absorbed onto the SA-crystal (Figure S3C).

Frozen nucleosome samples on SA-crystal grids were subjected to tomography data collection on a FEI Titan Krios transmission electron microscope, operated at 300 kV with an energy filter at 20 eV (Gatan BioQuantum). Tilt series were acquired with SerialEM (Schorb et al., 2019) using the automated data collection function, including fine eccentricity, item realignment, and autofocus scheme. The range for tomography collection was set from -60° to +60°, with an angular increment of 3° per tilting step. The target

defocus was set between 2.5-3 μm. The total electron dose for the whole tomography was calculated between 200 to 250 electrons per Å^2, with an adjustment of the exposure time following the 1/*cos* schemes. For each tilt angle, 8-10 frames were acquired every 0.25 s from 2 to 2.5 s of exposure using a Titan Krios Gatan K2/K3 camera with a pixel size of 1.45/1.47 Å.

Deep learning-based denoising

For deep learning denoising, we followed the description of the TOMO2TOMO (T2T) method (Buchholz et al., 2019). Frames of tilt angles were aligned using MotionCor2 (Zheng et al., 2017) to correct for image drift. Aligned frames were split into even and odd frame stacks and averaged separately to generate noise independent pairs for the same object. To select representative areas of the averaged image pair, 1,120 local box path-pairs of 600x600 pixels were generated at each apparent nucleosome core particle (NCP) position. Inside each NCP position, 10 patches of 128 × 128 pixels were further randomly cropped to train a CARE network in the NOISE2NOISE regime (Weigert et al., 2018). The neural network was constructed with a U-Net of depth two, a kernel size of three, one hundred training epochs, and a linear activation function at the last layer. The loss function was evaluated with a per-pixel mean squared error (MSE). After training, the network was applied to restore the full-size image pairs at each tilt. The final image of each tilt is the result of averaging two individual restorations of even and odd images.

Preprocessing of cryo-ET tilt series

The denoised tilt series were pre-aligned using the IMOD software package with the patch tracking method (Kremer et al., 1996). Then, further alignment was performed on the local image patches (200 x 200 pixels) by using the focused refinement strategy in individual-particle electron tomography (IPET)(Zhang and Ren, 2012). The alignment of the image tilt axis onto its central vertical axis allowed for the determination of the Contrast Transfer Function (CTF) of the microscope, using the GCTF software package (Zhang, 2016). CTF of the center slice of each micrograph and the cosine of the tilt axis angle were used to estimate the CTF of the flanking strip bands. Both the phase and amplitude were corrected for each strip band using TomoCTF (Fernández et al., 2006).

Cryo-ET 3D reconstruction and NCPs segmentation

To obtain the single-molecule 3D images, the CTF corrected tilt series were then submitted for a focused electron tomographic refinement (FETR) algorithm in IPET (Zhang and Ren, 2012) followed by 3D reconstruction using weighted Fourier back projection using the e2tomo software package (Chen et al., 2019; Tang et al., 2007a) without a further alignment step. The reconstructed maps were subjected to low pass (abs= 0.25), normalization and median shrink filters enhancement (bin= 8; pixel size= 11.68 Å). To implement the deep learning-based segmentation method in e2tomo, areas containing representative features for network training (crystal lattice, free distal DNA, NCPs, and background noise) were boxed out from z-dimensional slices of the reconstruction. The application of the trained network to the tomograms allowed for the segmentation of the NCPs, DNA, and SA crystals from the background. NCP segmentation was used as a marker to select surrounding connected map densities (within 10 Å) using the zonsel function of Chimera software (Pettersen et al., 2004). SA crystal segmentation was used as a marker to remove the surrounding SA crystal densities (within 10 Å). To produce a soft boundary mask for the missing wedge correction, the processed density maps were low-pass filtered to 30 Å and clipped to box of 512 x 512 x 200 pixels.

Missing wedge correction of 3D density map reconstruction

To reduce the tilt limitation caused the elongation artifact in the 3D reconstruction, the missing wedge correction was performed by the low-tilt tomographic reconstruction (LoTToR) method (Zhai et al., 2020), which is a model-free iterative process, under a set of constraints in the real and reciprocal spaces, aiming to fill the missing wedge zone in Fourier space. To implement the algorithm, a soft boundary 3D mask was generated using the previously denoised density map after 30 Å low-pass filtering. This 3D mask was paired with the initial 3D reconstruction to generate nine cubic tiles of 200 x 200 x 200 pixels with overlapping regions of 30 x 200 x 200 pixels as reference for realignment. These cubic tiles were subjected to iterations of the missing wedge correction until the final corrected 3D map converged with a stable Fourier shell correlation value. The final 3D density map of 512 x 512 x 200 pixels was re-assembled by aligning the corresponding missing wedge corrected density cubes.

Modelling of the final denoised 3D electron density map

A 3D global template-matching was obtained by competitively docking the nucleosome model (PDB ID:1AOI) and a linear 40 bp DNA model into the final missing wedge corrected density map. This procedure consisted of four major steps: i) NCP segmentation maps were split into domains using the watershed method of Chimera (4 smoothing steps with a step size of 3 voxels). High-density weight centers of each domain were calculated at different map contour levels (from 1090% of its maximum in a step of 0.5). ii) NCP and 40 bp DNA models were fitted into the weight centers with a random rotation. iii) The competitive docking of positioned NCP and DNA models was determined using the sequential multi-model fitting function in Chimera (Pettersen et al., 2004). All docked models were ranked based on the cross-correlation value (CC-score) between the models and the map. Models with either a CC-score < 0.7 or exhibiting a clash event with higher-ranked models were removed from the analysis. iv) Steps ii) and iii) were repeated multiple times until a stable fitting was identified as explained below.

A stable fitting of each map domain was obtained by the process of maximizing the average CC-score and minimizing the map/model fitting residue (MaFR/MoFR). MaFR corresponds to the remaining density volume after subtracting the combined model from

Molecular Cell
Article

CellPress
OPEN ACCESS

the density map, and MoFR corresponds to the remaining density volume after subtracting the density map from the combined model. A score to evaluate the minimization of the fitting residue compared the current fitting with the best previous fitting and was defined as the ratio between $(MaFR_{current} - MaFR_{best})/MaFR_{best}$ and $(MoFR_{current} - MoFR_{best})/MoFR_{best}$. A negative value of both $(MaFR_{current} - MaFR_{previous})$ and $(MoFR_{current} - MoFR_{previous})$ indicated that a better fitting was found. A score threshold of < -0.1 was set to accept the current fitting as the best fitting. The fitting loop was stopped when no better fittings were found in ten consecutives iterations. The translations and rotations of each NCP and DNA linker models were recorded for the statistical analysis described in the following sections.

A 3D particle stack was generated by cropping out identified NCPs within the tomograms. This particle stack was submitted to the e2tomo program (Chen et al., 2019) for sub-tomogram averaging in order to further validate the quality of the selected nucleosome particles. We carried out the 3D refinement routine with a single featureless discoidal-shaped initial model (niter= 3, sym= c1, and without masks), and calculated 3D averaging for different fractions of particles (pkeep= 1.0, 0.8, 0.6, and 0.4). The map resolutions were estimated by measuring the Fourier shell correlation (FSC) between two independently determined half-maps and between map and crystal structure 1AOI when the coefficient fell below 0.5 and 0.143.

QUANTIFICATION AND STATISTICAL ANALYSIS

Identification of free and condensed NCPs

The weight centers of NCPs in the fitted model were classified based on their distance from their neighbors, using the density-based spatial clustering of applications with noise algorithm (DBSCAN) (Ester et al., 1996). DBSCAN required two input parameters, *eps* and *min_samples*, where *eps* defines the maximum distance between two points to be considered as neighbors, and *min_samples* defines the minimum number of neighbors to be considered as clusters. An initial classification to identify free NCPs and condensates was performed using an *eps* value of 250 Å, which is the minimum theoretical distance between two consecutive nucleosomes in the same array (2 x 55 Å NCP (disc radius) + 40 bp DNA x 3.4 Å/bp= 250 Å), and a *min_sample* value of 8, which is, by definition, the smallest cluster composed of two tetranucleosome units. A second classification was performed based on the previous classification, using an *eps* value between 270-290 Å, and a *min_sample* value of 12. This produced a cleaner segmentation that differentiated free NCPs from NCPs grouped in condensates, representing the light and dense phase of spinodal decomposition, respectively. In the case of small SphCs that interact among themselves or with irregular condensates, a subclassification was manually performed to distinguish each SphC within the cluster.

Calculation of tetranucleosome condensates geometry

The shape of irregular and spherical nucleosome condensates was determined by measuring its physical dimensions and eccentricity. The condensate dimensions are represented by the length of its long and short axis. The direction of the long and short axis was calculated using the coordinates of the center of mass of NCPs and the principal component analysis (PCA)(Pearson, 1901) which produced the vector PC1 for the long axis and the vector PC3 for the short axis. The lengths of the long and short axis were calculated as the distances between the two most separated NCPs along the PC1 and PC3 vectors. The overall size of the condensate was estimated by averaging the length of the long and short axis. The eccentricity was calculated using the formula "1- (short axis length / long axis length)" which yielded a score between zero and one, where zero represents a perfect spherical shape, and one represents an elongated structure.

Calculation of NCP condensate boundary sharpness

To define the overall shape of the condensates, a boundary mask was produced using the electron density of condensates with a 10 nm low-pass filter. To calculate the surrounding free NCPs concentration, which represents the condensate boundary sharpness, a shell of 20 nm extending from the boundary mask was established to determine the number of the surrounding free NCPs, which in turn was divided by the volume of the external 20 nm shell.

Determination of NCP concentration in condensates

The nucleosome ice-slab (global) concentration for the early stage of phase separation (when light phase and dense phase are formed under ~100 nm scale) was calculated by dividing the total number of NCP within the tomogram by the volume of the smallest cuboid that enclosed all NCPs. To measure the concentration of NCPs in SpnCs and SphCs, an initial condensate-shaped mask was produced based on the electron density after a 10 nm low-pass filter, and a series of 3D contours were established either by shrinking or expanding the mask in steps of 2 nm. The innermost contour was labeled as *n*= 1, and the next consecutive contour was labeled as *n* + 1. A shell defined as the 3D space between two consecutive contours was also labeled starting from inside the condensate (*n*= 1). To calculate the concentration of NCPs inside a specific contour *c*, the number of NCPs within contour *n* was divided by the volume enclosed by the contour. To calculate the concentration of NCPs inside a specific shell *n*, the number of NCPs within the shell *n* was divided by the volume of the shell. To avoid double counting NCPs that cross two shells or contours, the center of mass of NCP was used to determine its residing shell or contour. The mean NCP concentration was obtained by averaging the NCP concentration inside a specific contour or shell *n* at the same position in the same type of condensates. Since condensates vary in size, the total number of contours within a condensate differ from each other, which may cause more variance in concentration measurements for the exterior contour/shell.

CellPress
OPEN ACCESS

Molecular Cell
Article

Calculation of the pair distribution function (*g(r)*) of NCPs within condensates

The *g(r)* function was determined using the distribution of the pairwise distances between the weight centers of NCPs. For each NCP weight center, a series of spheres separated by 1.6 nm (*dr*; small step of radius extension) were generated using a radius (*r*) ranging from 0 to 60 nm. This resulted in shells formed by two consecutive concentric spheres (i.e., the shell between *r* and *r* + *dr* away from the reference NCP weight center). The NCP density of each shell was calculated by dividing the number of NCPs within the shell by the shell volume ($4\pi r^2 \times dr$), and the shell densities of different spheres with the same radius were averaged and divided by the ice-slab (global) density for normalization. However, the shell density estimation for NCPs that reside at the border of the tomography is not accurate. To correct this, a periodical boundary was applied to the *x*- and *y*-direction of NCP models, lengthening the respective dimensions of the tomogram 2-fold. If the shell surpasses the *z*-direction boundary of the tomogram, a correction factor (the ratio between the overall shell volume and the partial shell volume inside the tomogram) was multiplied with the corresponding shell density because the *z*-direction is non-extensible, due to having contact with ice (top) and the SA-crystal surface (bottom). For tomograms containing SphCs, only the condensate region was selected for *g(r)* analysis, and due to the large background density variation among different condensates, the *g(r)* density was normalized by setting the highest peak equal to one.

Calculation of the NCPs orientation within condensates

To calculate the orientation of NCPs on the surface and in the interior of different types of condensates, each NCP within the fitted model was simplified as a triangular shape centered on the nucleosomal discoidal plane. For SphCs, the orientation of each NCP relative to its containing condensates was measured as θ which is the angle between the triangular plane and the radius of the condensate that crosses the triangle center (i.e., the center of mass of NCP). Similarly, for an irregular-shaped condensate with a radius that cannot be define, θ was measured as the angle between the triangular plane and the line perpendicular to the spine of the condensate crossing the triangle center. To calculate the spine of the condensate, the density map of the condensate was eroded to irregular lines by using Lee's 3D skeletonizing algorithm (Lee et al., 1994). The θ angle distribution of NCPs for each type of condensate was evaluated by comparison with a $cos(\theta)$ function, which represents a randomly distributed orientation of NCPs. The $cos(\theta)$ represents the distribution of orientations of random unit vectors relative to a fixed plane, which in turn was equivalent to the probability of finding a point on the unit hemisphere contained in a differential ring-shape area: $P(\theta)d\theta = 2\pi(Rcos(\theta))Rd\theta/2\pi R^2 = cos(\theta)d\theta$.

Supplemental information

Molecular organization of the early stages

of nucleosome phase separation

visualized by cryo-electron tomography

Meng Zhang, César Díaz-Celis, Bibiana Onoa, Cristhian Cañari-Chumpitaz, Katherinne I. Requejo, Jianfang Liu, Michael Vien, Eva Nogales, Gang Ren, and Carlos Bustamante

A Magnification 50,000 X

36°C
20°C
4°C

150 nm

2 min   10 min   30 min   60 min   90 min

B NCP Grid Surface Density

Density (μm⁻²)

Temperature
4°C
20°C
36°C

Time (min)

SphC Grid Surface Density

Density (μm⁻²)

Temperature
4°C
20°C
36°C

Time (min)

C Low salt (1.5 mM Na⁺) 2 min

Physiological salt 2 min

Irregular condensates

100 nm

D Physiological salt 10 min

Globular condensates

100 nm
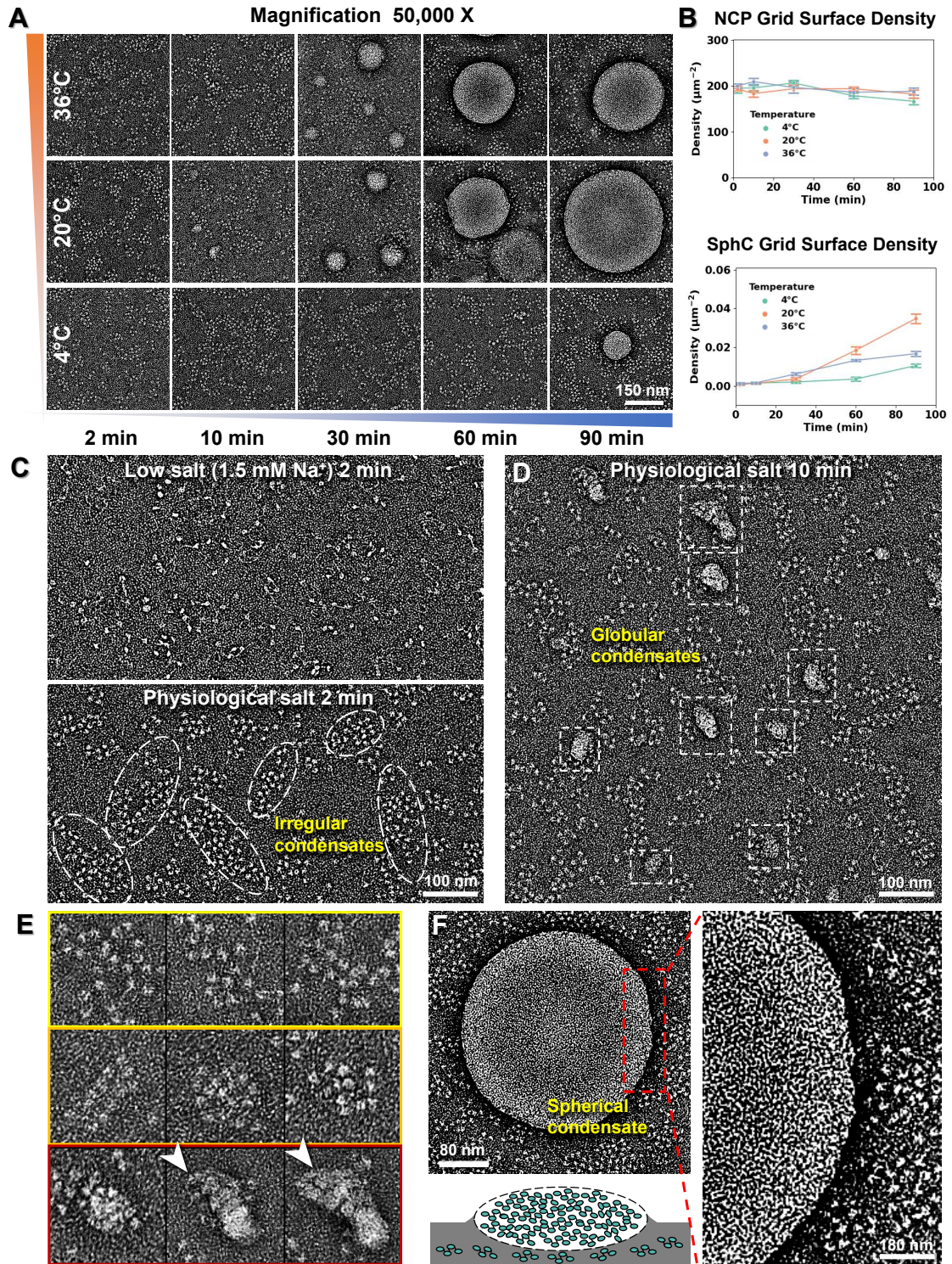
E

F Spherical condensate

80 nm

180 nm

Figure S1

Figure S1. Tetranucleosome phase transition visualized by OpNS and epifluorescence imaging, related to Figures 1, 2, 3, and 4

(A) Representative time series of 30 nM tetranucleosome in physiological salt (20 mM HEPES-KOH pH 7.5; 150 mM NaCl; 5 mM $MgCl_2$; and 1 mM DTT) at 4°C, 20°C, and 36°C imaged at magnifications of 50,000 X. (B) Statistics of nucleosome number density (number of nucleosomes within irregular condensates divided by the corresponding imaging area) and SphC number density measured from figure S1A. Data was obtained from 12-16 12,500 X images and statistics are presented as mean ± SEM. (C) Tetranucleosomes visualized by OpNS in low salt (1.5 mM Na^+, top) and physiological salt (bottom) after 10 min incubation at 20°C. Dashed-line ellipsoids enclose condensates displaying an irregular shape and loosely packed nucleosomes. (D) Tetranucleosome condensates formed in physiological salt buffer after 10 min incubation at 20°C. Dashed-line boxes mark globular condensates displaying tighter nucleosomal packaging. (E) Representative images of nucleosome clusters in physiological salt showing different degrees of condensation from loosely packed structures to tightly packed condensates (top to bottom). Box size= 100 nm. (F) OpNS image of a SphC (left top panel) stained after 90 min, whose edge has been enlarged (right panel) to see the tightly packed nucleosomal pattern on its surface. The high density of the SphC prevents visualization of its interior and the irregular condensates below it as depicted in schematic (bottom panel).
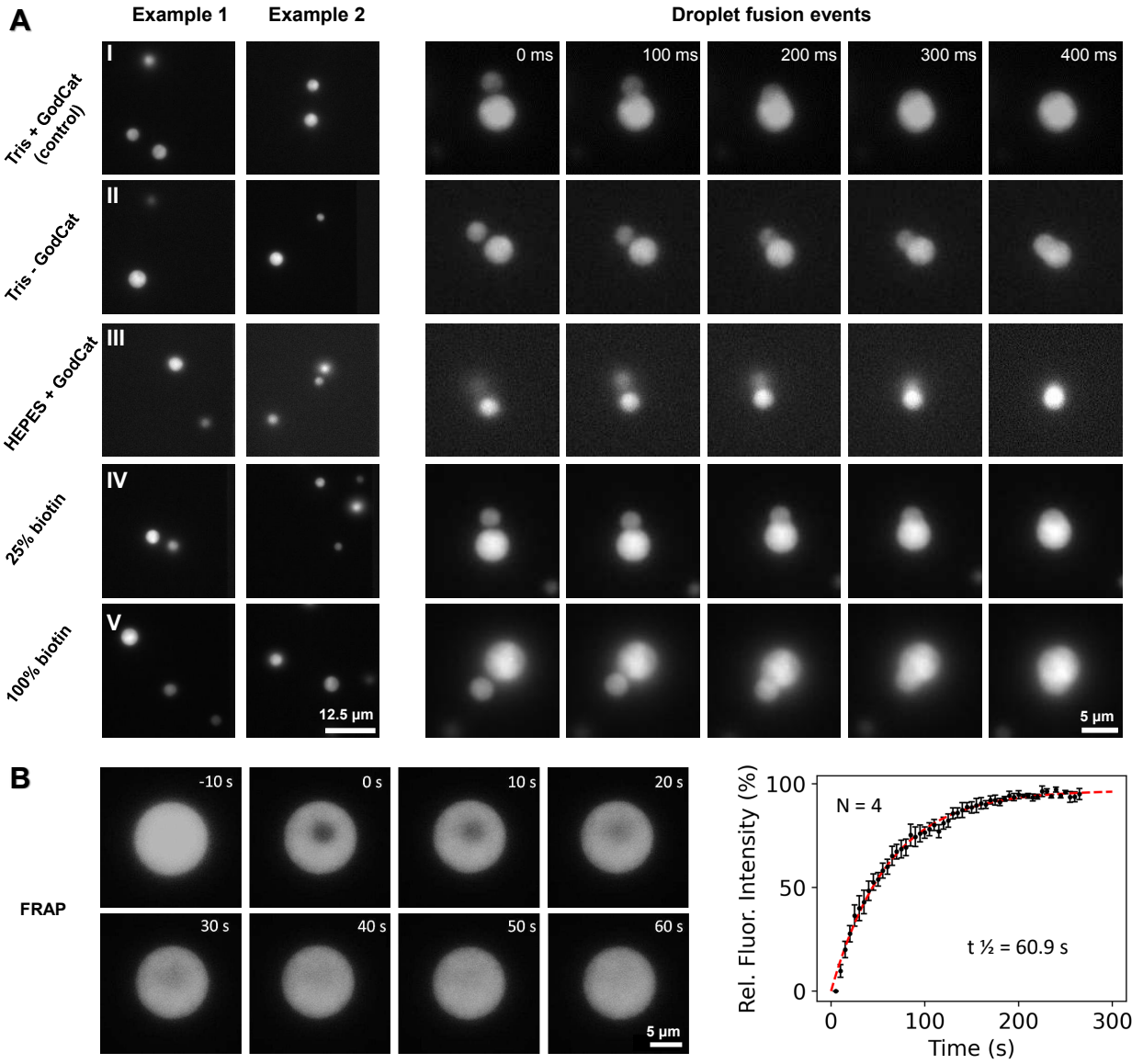
Figure S2

Figure S2. Tetranucleosome condensation observed by epifluorescence microscopy, related to Figures 1, 2, 3, and 4

(A) Fluorescence microscopy imaging of Cy3-labeled nucleosome liquid droplets formed in physiological salt and the observed fusion events. The glass surface was passivated with BSA for all the conditions tested. Images were taken after 1 h of condensate formation at room temperature. (I) Tetranucloesome in 50 mM Tris-HCl pH 7.5, 150 mM NaCl, 5 mM MgCl$_2$, 1 mM DTT, and using the GodCat oxygen scavenging system. (II) Tetranucloesome in 50 mM Tris-HCl pH 7.5, 150 mM NaCl, 5 mM MgCl$_2$, 1 mM DTT, without the GodCat oxygen scavenging system. (III) Tetranucloesome in 20 mM HEPES-NaOH pH 7.5, 150 mM NaCl, 5 mM MgCl$_2$, 1 mM DTT, and the GodCat system. (IV) Tetranucloesome condensation using a 3:1 ratio (25%) of non-biotinylated to biotinilylated tetranucleosome DNA template, in 50 mM Tris-HCl pH 7.5, 150 mM NaCl, 5 mM MgCl$_2$, 1 mM DTT, and using the GodCat oxygen scavenging system. (V) Tetranucloesome condensation using a 100% biotinilylated tetranucleosome DNA template, in 50 mM Tris-HCl pH 7.5, 150 mM NaCl, 5 mM MgCl$_2$, 1 mM DTT, and using the GodCat oxygen scavenging system.   (B) Fluorescence recovery after partial photobleaching of Cy3-labeled tetranucleosome droplets formed in physiological salt after 1 h incubation at 20°C. The nucleosome diffusion coefficient within the droplet was determined by measuring the averaged rate of change of relative fluorescence intensity.

A

Dodecamer nucleosome array

100 nm

100 nm

B

Magnification 50,000 X

2 min

10 min

30 min

60 min

90 min

C

10 min incubation   1 h incubation

Charged carbon grid

Imaging area

Carbon area

SA-crystal grid

Imaging area

Carbon area

1 μm

D

Ionic strength

5 mM Mg²⁺

150 mM Na⁺

5 mM Mg²⁺
150 mM Na⁺

0.5 mM Mg²⁺

15 mM Na⁺

5 mM Mg²⁺
15 mM Na⁺

0.05 mM Mg²⁺

1.5 mM Na⁺

5 mM Mg²⁺
1.5 mM Na⁺

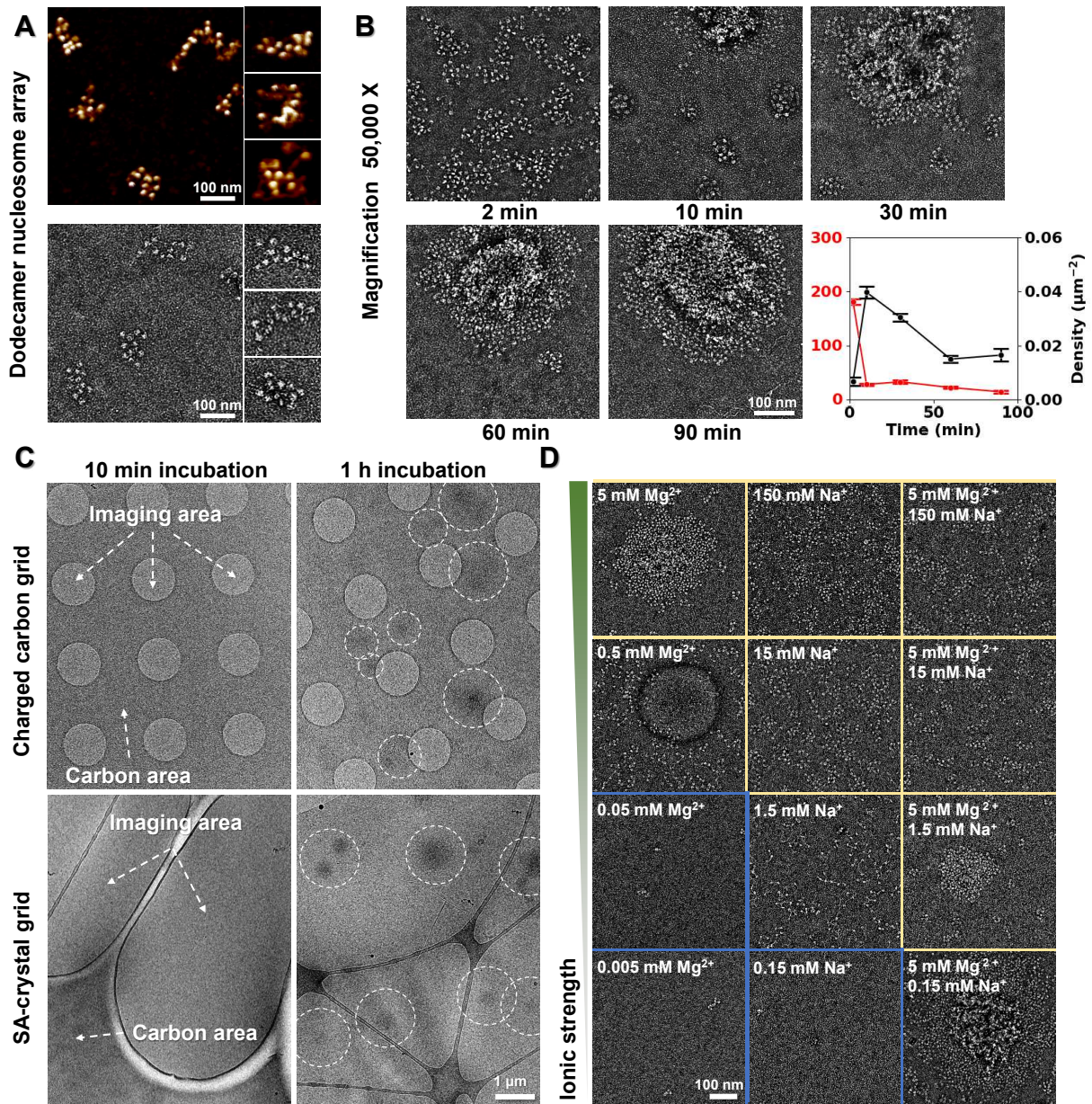0.005 mM Mg²⁺

0.15 mM Na⁺

5 mM Mg²⁺
0.15 mM Na⁺

100 nm

Figure S3

Figure S3. Measurement of condensates inner diffusion coefficient, size variation, grid surface density, and morphology, related to Figures 1, 2, 3, and 4

(A) AFM and OpNS images of dodecamer nucleosome array and representative particle views (box size 100 nm). (B) Time series of 10 nM dodecamer nucleosome array in physiological salt at 20°C imaged at magnifications of 50,000 X. Statistics of nucleosome and SphC number density shown in red and black, respectively. Data were obtained from 12-16 12,500 X images and statistics are presented as mean $\pm$ SEM. (C) Cryo-EM sample of tetranucleosomes prepared using the conventional glow discharged carbon quantifoil grid (left panel) and the non-charged SA-crystal lacey grid (right panel) after 10 min and 60 min incubation. Dashed line circles indicate large-scale condensates favored the binding to the carbon (non-imaging) area of conventional grid (left). However, similar size condensates were observed in the vitreous ice (imaging) area using a SA-crystal grid (right). (D) Effect of Mg^{2+} concentration on condensate formation (20 mM HEPES-KOH pH 7.5; 5-0.005 mM $MgCl_2$; and 1 mM DTT, left column). Effect of Na^+ concentration on condensate formation (20 mM HEPES-KOH pH 7.5; 150-0.15 mM NaCl; 1 mM EDTA; 1 mM DTT, middle column). Effect of Na^+ concentration on condensate formation at constant Mg^{2+} concentration (20 mM HEPES-KOH pH 7.5; 150-0.15 mM NaCl; 5 mM $MgCl_2$; and 1 mM DTT, right column). Low ionic strength buffer decreases nucleosome adsorption to the grid surface (Blue section) in contrast with high ionic strength buffer (yellow section). In D, all tetranucleosome samples were incubated 10 min at 20°C before OpNS.
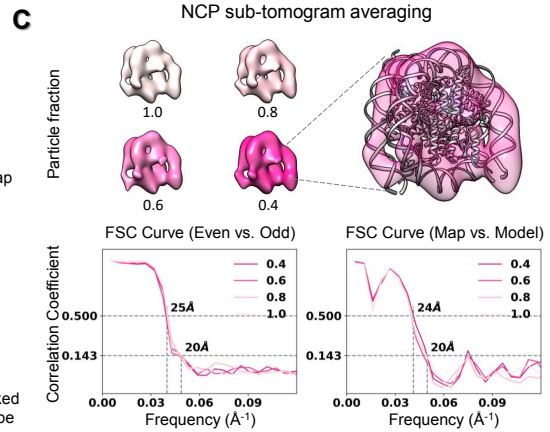
A

Local movie frames

1120 local patches

even

odd

T2T training

Apply CNN

CTF Corr.

Large tilt image

IMOD tilt series alignment
IPET local refinement

3D segmentation

SA-Crystal

Raw — Positive — Negative

Target

Prediction

NCP

Raw

Target

Prediction

Flanking DNA

Raw

Target

Prediction

Raw 3D reconstruction

− marker

+ marker

+ marker

Raw 3D reconstruction

CNN based annotation

LottoR MW correction

NCP Mask

Local patches

200x200x200 box

Dissembling

Local low-passed masks

Reassembling

Correction results:
Cubics from an overlapped area

B

Early-stage Irregular condensates
Intermediate-stage irregular condensates
Late stage irregular condensates
Small spherical condensates
Grown Spherical condensates
H1-grown spherical Condensates

Density

Tomo. 1   0.8   0.82   0.82   0.79   0.79   0.77

Tomo. 2   0.81   0.82   0.8   0.81   0.77   0.8

Tomo. 3   0.81   0.82   0.8   0.81   0.79   0.78

Tomo. 4   0.81   0.82   0.83   0.81   0.8   0.79

cc value

cc= 0.96   cc= 0.36

NCP Crys. Map   DNA Crys. Map

NCP Fitting Model

cc= 0.30   cc= 0.67

3D Noise   3D Noise masked by a NCP shape

C

NCP sub-tomogram averaging

Particle fraction

1.0   0.8

0.6   0.4

FSC Curve (Even vs. Odd)

Correlation Coefficient

0.500

0.143

25Å

20Å

0.4
0.6
0.8
1.0

0.00   0.03   0.06   0.09

Frequency (Å⁻¹)

FSC Curve (Map vs. Model)

0.500

0.143

24Å

20Å

0.4
0.6
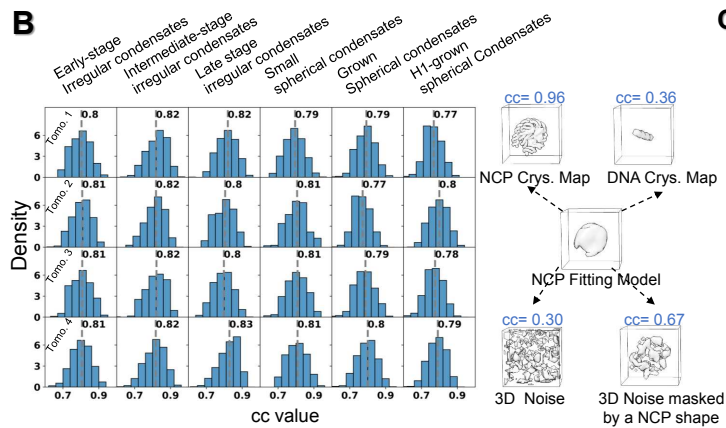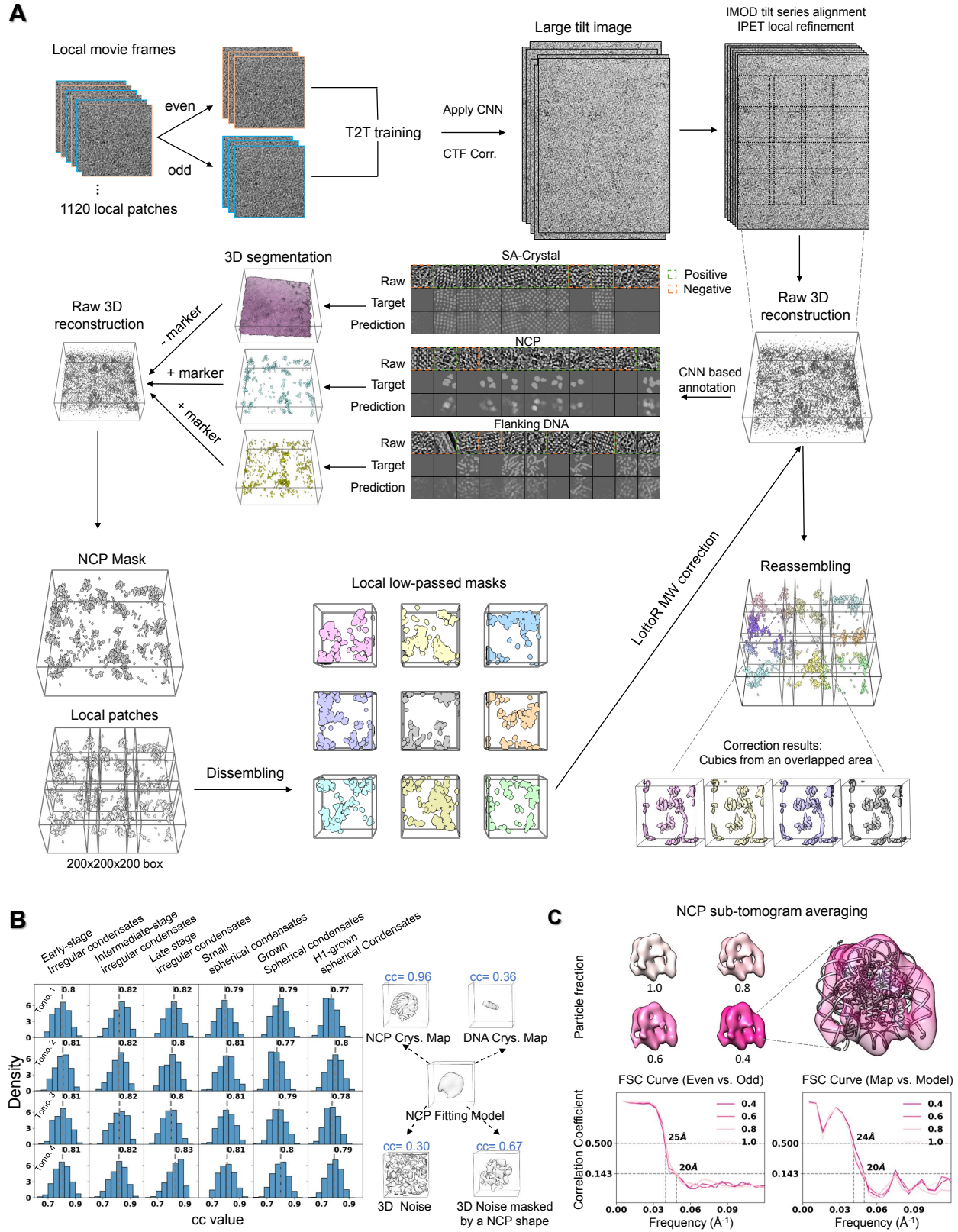0.8
1.0

0.00   0.03   0.06   0.09

Frequency (Å⁻¹)

Figure S4

Figure S4. Tomogram reconstruction work flow and validation of identified NCPs, related to Figure 1

(A) The tomographic 3D reconstruction work flow from the tilt series. The denoised tilt series using the TOMO2TOMO (T2T) method were initially aligned and locally refined by individual particle electron tomography (IPET) (top row). Annotation of the 3D reconstructed tilt series (middle row). Resulted NCP and DNA segments were used as markers to select the nucleosome array density in raw map. Local low-tilt tomographic reconstruction (LoTToR) based missing wedge (MW) correction after dissembling 3D map into patches (bottom row). MW corrected patches were resembled by aligning the overlap area. (B) Histograms showing the map-model fitting score distributions of all identified NCPs for four representative cryo-ET reconstructions (rows) from different types of condensates (columns) (left panel). The fitting scores were calculated by measuring the cross-correlation between the local density map and the corresponding model. Evaluation of the cross-correlation coefficient between NCP fitting model and reference models (right panel). A score of 0.96, 0.36, 0.30, and 0.67 were obtained for the NCP crystal structure map, DNA crystal structure map (40 bp), random noise map, and random noise enclosed by an NCP-shaped map, respectively. (C) Quality evaluation of the identified NCPs by sub-tomogram averaging method. The density maps averaged from different fractions (1.0, 0.8, 0.6 and 0.4) of NCP particles and model fitting (Top). The map resolutions were estimated by measuring the Fourier shell correlation (FSC) between two independently determined half-maps and between map and crystal structure 1AOI (bottom).

A Cluster eccentricity

B Concentration of Free NCPs

C Total concentration of NCPs

D Average Cluster Size

E Example 1   Example 2   Example 3   Example 4

t2-LS

t2-PS

t10-PS

Box size = 600 nm

F Pair-wised correlation matrix

r=-0.8

r=0.8   r=-0.7

r=0.9   r=-0.7   r=0.8

r=0.8   r=-0.6   r=0.7   r=0.5

Figure S5

Figure S5. Statistical analysis of cluster shape, concentration, distance, size, and correlations for irregular condensates obtained from the cryo-ET reconstruction, related to Figure 2

(A) Quantitation of irregular condensates eccentricity expressed as (1 – PC3/PC1). (B) Concentration of free NCPs within the ice slab (number of free NCPs divided by the ice volume of the reconstructed tomogram). (C) Total NCP concentration within the ice slab (number of all identified NCPs divided by the ice volume). (D) Average dimensions of irregular condensates expressed as a mean between the long (PC1) and short (PC3) axes obtained from a Principal Component Analysis (PCA). All data are plotted as mean ± SEM and measurements are compared using a two-tailed unpaired t-test, where $*p < 0.05$, $**p < 0.01$, $***p < 0.001$, $****p < 0.0001$; ns, not significant. (E) Measurement of the nearest neighbor distance among irregular condensate clusters. Identification of condensate-shaped contours (blue dots) within the z-dimension central slice for early (t2-LS), intermediate (t2-PS), and late irregular (t10-PS) condensates (top to bottom). Four examples of these three conditions are presented (columns). Nearest-neighbor condensates are connected by green lines, whose mean distances were used to represent the change of the critical wavelength, describing the evolution of spinodal decomposition in time. (F) Pairwise correlation matrix between independently determined number of NCPs per condensate, condensate size, eccentricity, neighbor distance among condensates, and concentration of free NCPs surrounding condensates. The mean values of the above five independent measurements from tomograms obtained for early, intermediate, and late stage irregular condensates are presented in green, orange, and blue points, respectively. The analysis yielded a mean Pearson correlation coefficient (r-value) of 0.73.
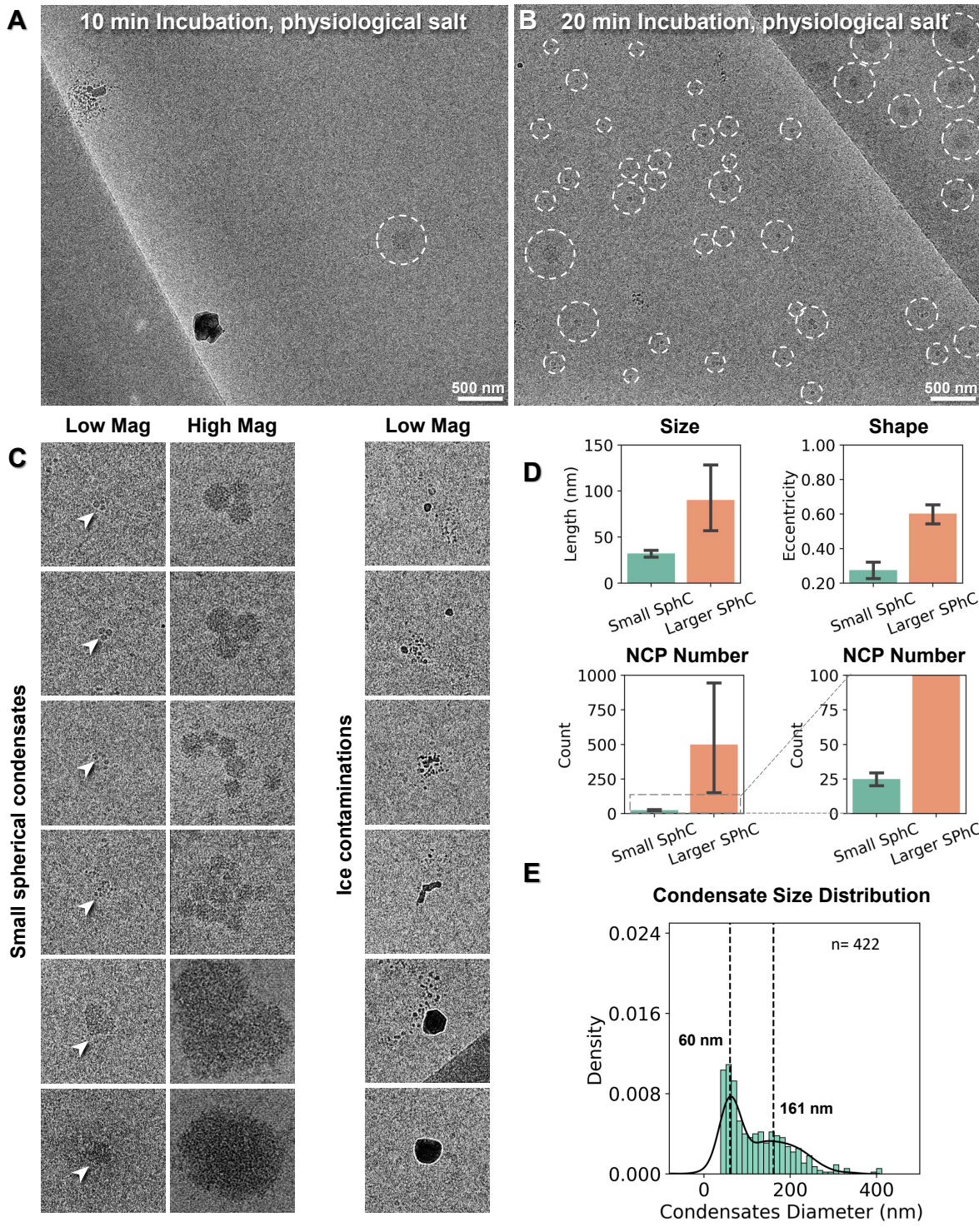
A 10 min Incubation, physiological salt

B 20 min Incubation, physiological salt

500 nm

500 nm

C

Low Mag   High Mag   Low Mag

Small spherical condensates

Ice contaminations

D

Size

Shape

NCP Number

NCP Number

E

Condensate Size Distribution

n= 422

60 nm

161 nm

Density

Condensates Diameter (nm)

Figure S6

Figure S6. Identification of small SphCs and quantitation of their size, shape, and distribution from 2D cryo-EM images and 3D reconstructions, related to Figure 4

(A) Representative cryo-EM image showing the sparsely distributed SphCs on the SA-crystal surface after 10 min incubation in physiological salt at 20°C. (B) Representative cryo-EM image showing small SphCs of varying sizes under the same condition as A after 20 min incubation. (C) Representative particle views of a small and a larger bundle of attached small SphCs imaged at both low (3,600 X) and high (53,000 X) magnification (left). Control images of ice contaminants showing a high contrast and white particle fringe when compared to nucleosome condensates at similar sizes (right). Ice particles were excluded from the statistical analysis of small condensate size distribution. Box size for Low Mag= 1,000 nm; Box size for High Mag= 220 nm. (D) Statistical analysis of the size (defined as the mean of the PC1 and PC3 axes after PCA analysis), eccentricity (1 – PC3/PC1 axis), and number of containing NCPs of small (n= 27) and larger (n= 7) SphCs measured from the reconstructed tomogram 3D models. (E) Histogram of SphC size distribution measured from low magnification 2D cryo-EM images (B; n= 440). Data were fitted using two Gaussians distributions. Dashed lines correspond to the mean of the two distributions (60 and 161 nm).
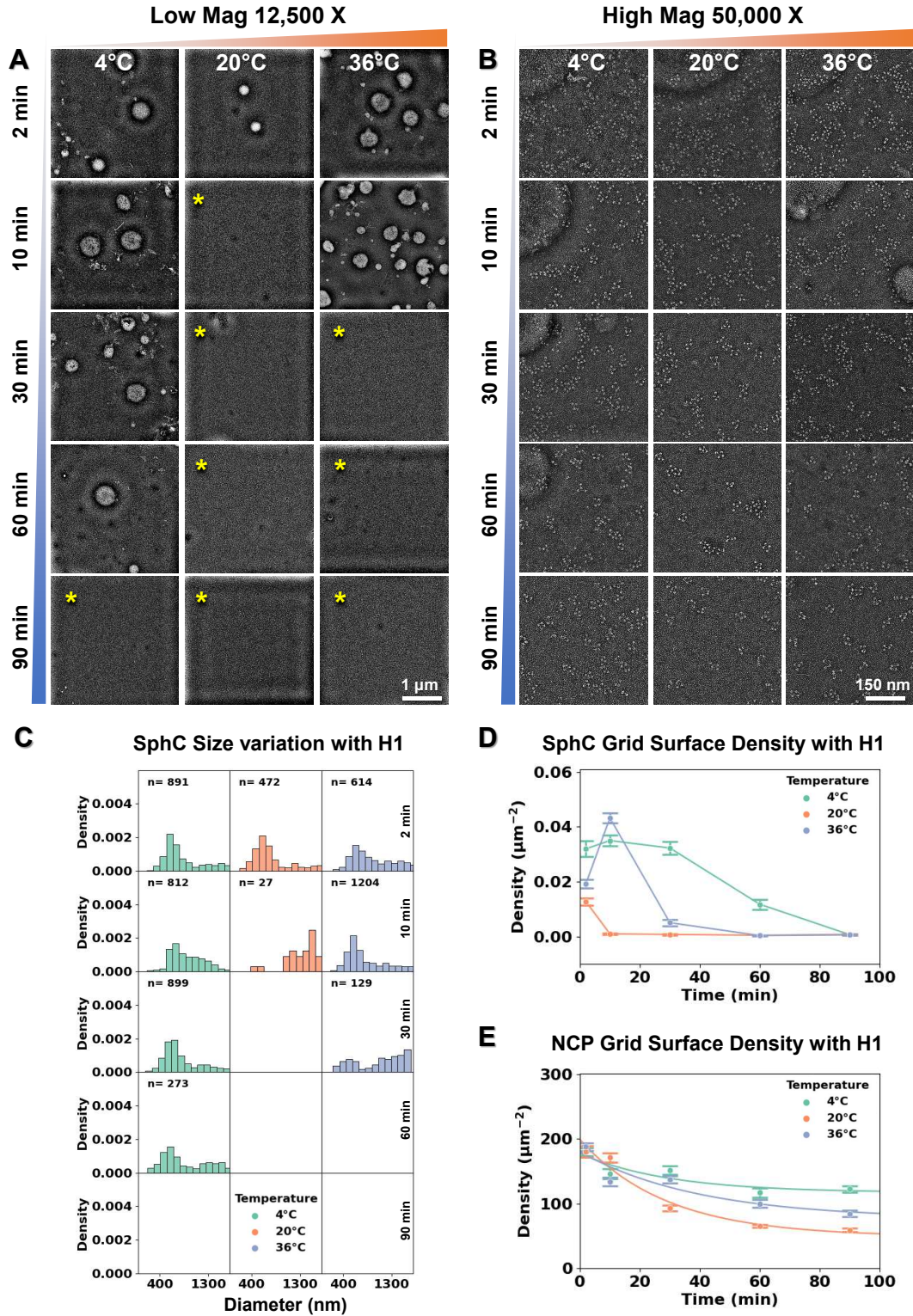
Low Mag 12,500 X

High Mag 50,000 X

A

B

C — SphC Size variation with H1

D — SphC Grid Surface Density with H1

E — NCP Grid Surface Density with H1

Figure S7

Figure S7. Quantitative measurement of size variation and grid surface density of tetranucleosome condensates in the presence of H1, related to Figure 5

Representative time series of 30 nM tetranucleosome in physiological salt and 120 nM H1 at 4°C, 20°C, and 36°C imaged at magnifications of (A) 12,500 X; and (B) 50,000 X. (C) Statistics of SphC size distribution on the carbon grid surface in the presence of H1 measured from A. (D) Statistics of SphC density on the carbon grid surface in the presence of H1 (number of condensates divided by the imaging area) measured from A. (E) Statistics of nucleosome density in the presence of H1 (number of nucleosomes within SpnCs over the corresponding imaging area) measured from B. Data C-E was obtained from 12-16 images and statistics are presented as mean ± SEM. Data in E were fitted with an exponential decay function. The low chance of observing SphCs on the grid surface after longer incubation (yellow asterisk in A) is a feature observed in the presence of H1, which produced larger but fewer SphCs given the limited amount of nucleosome material in solution. This inference is supported by 1) the SphC grid surface number density decreased over time in D; 2) a significant amount of spinodal material was depleted after 90 min of reaction in E; 3) the disappearance of SphC at earlier time points is consistent with a faster material depletion rate (20°C > 36°C > 4°C in E). Due to the difficulty in binding to carbon grid surface, large SphCs over >1.8 μm were not observed in all conditions.
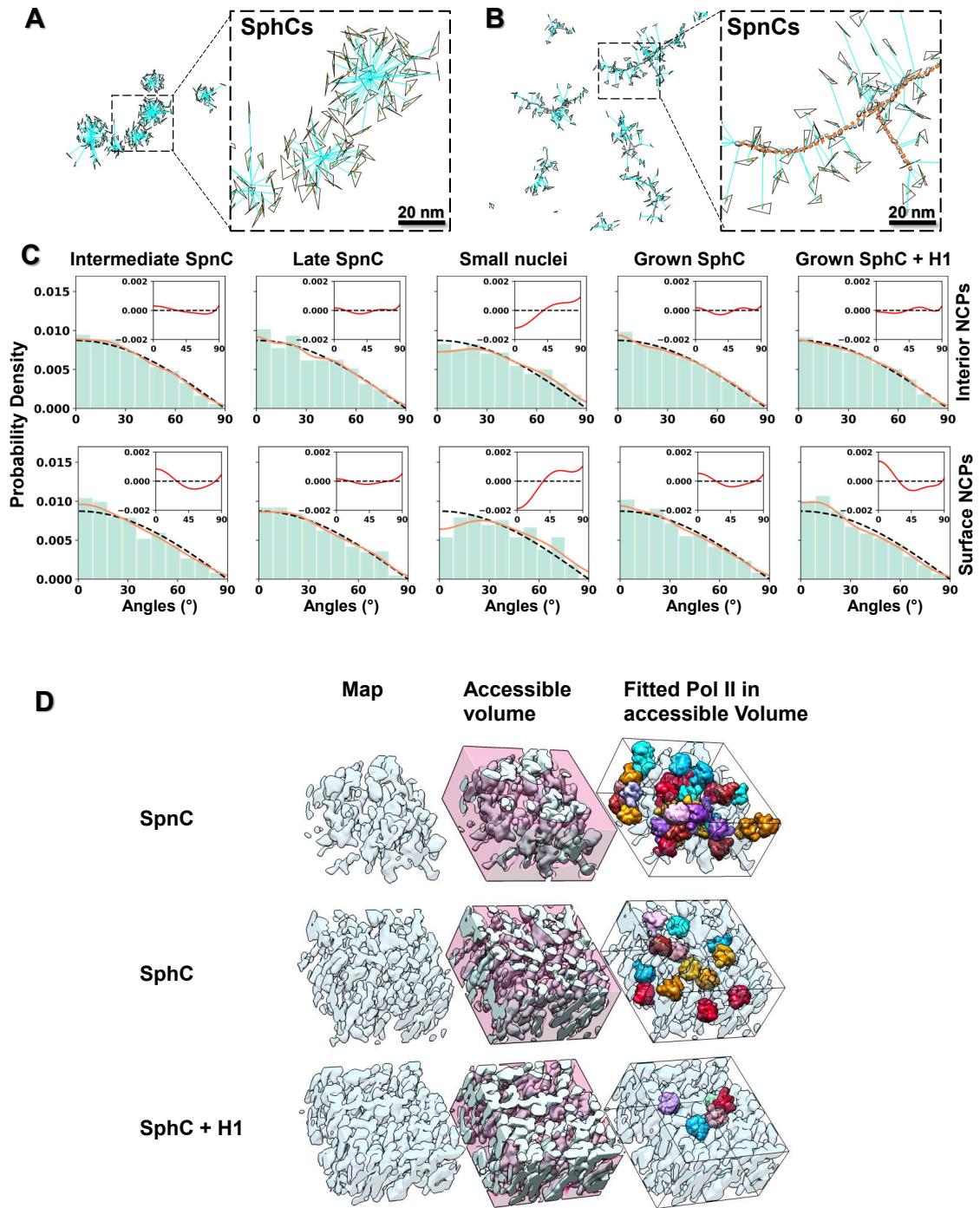
Figure S8

Figure S8. Quantitative analysis of NCP orientations and evaluation of chambers capacity for different types of condensates, related to Figure 6

(A) Angle (θ) measurement of NCP disk plane (black triangle) relative to the radius of the SphC (cyan line) that crosses the center of the triangle (left panel). The zoom-in view is shown on the right panel. (B) Angle (θ) measurement of NCP disk plane relative to the radial line (cyan line, which is perpendicular to the axial axis of SpnC) that crosses the center of the triangle (left panel). The axial axis of the SpnC was determined as the skeleton of the map (orange dashed-line, on the right panel). (C) Histogram of NCP disk angle distribution in the interior (top row) and on the surface (bottom row) of the condensates. The angle distribution was fitted with an 8th power polynomial (orange dashed line) and compared with a *cos*(θ) function (black dash line represents the angle distribution of a random rotated plane against a fixed axis). The deviation of experimental measurements from the *cos* was plotted on the top insets (red curves) indicating the preferred NCP disk orientation found within each type of condensate. (D) Evaluation of chambers capacity for RNA Polymerase II (Pol II) for different types of condensates. Sampling volumes of 2.88 x 10^5 nm^3 (first column) from the final density maps of late stage SpnCs, SphCs, and SphCs in the presence of H1 (from top to bottom rows, respectively) were inverted and 3 nm low-pass filtered to show the detected empty chambers (second column, pink region). The capacity of the chambers was evaluated by quantitating the number Pol II molecules that fit within each condensate (third column, each Pol II was labeled with a random color). The number of Pol II molecules contained in the chambers from the late stage SpnCs, SphCs without and with H1, was 38,13, and 5, respectively.

A. Theory of liquid phase separation

Phase separation is a non-equilibrium thermodynamic process in which a uniformly mixed system can lower its free energy (G) by segregating into two or more phases with distinct compositions that reach chemical equilibrium. The conditions at which distinct phases occur and coexist at equilibrium are described in a phase diagram. How do these conditions fulfill minimization of free energy (G) and satisfy the criteria for phase equilibrium? For a binary system exhibiting phase separation, the Gibbs free energy of a two-component solution as a function of composition exhibits a region of downward concavity or a negative curvature $\left(\frac{\partial^2 G_{solution}}{\partial x_B^2} < 0\right)$ in which the mixed system is unstable (Figure S9A). In this instability region, the single-phase system spontaneously undergoes demixing into two phases α and β, whose compositions must fulfill the criterion for phase equilibrium, i.e., that the chemical potential of each component of the binary mixture is the same in both phases (See equation 1, part B). Since the chemical potential of component *i*, μ_i, is the first derivative of the free energy with respect to the concentration of component *i*, n_i, the equilibrium condition implies that $\mu_i{}^\alpha = \frac{\partial G}{\partial n_i} = \mu_i{}^\beta$, which can be obtained graphically at every temperature by finding the concentrations of both components for which the free energy has a common tangent (Figure S9A) (Clerc and Cleary, 1995). The common tangent defines the points of the binodal curve, (Figure S9B) which, in turn, defines the end point composition of phase separation, which may occur by different mechanisms.

Spinodal Decomposition vs Nucleation and Growth

At compositions where $\left(\frac{\partial^2 G_{solution}}{\partial x_B^2} < 0\right)$, the mixed or single-phase system is unstable to both small and large fluctuations in composition. In this case, phase separation takes place without having to cross an energetic barrier and, therefore, it will occur throughout the entire system in a process known as spinodal decomposition (Figure S9B). A detailed description of the equations involved in spinodal decomposition first

formulated by Cahn and Hilliard (Cahn and Hilliard, 1958, 1959) is presented in the part B.

On the other hand, in the region in which the free energy as a function of composition has a positive curvature $\left(\frac{\partial^2 G_{solution}}{\partial x_B{}^2} > 0\right)$ (Figure S9A), the mixture is said to be metastable; in this region, phase separation only happens in discrete locations throughout the mixture where some rare, large fluctuations in composition spontaneously occur, because the system must overcome an energetic barrier. These localized regions, which appear sparsely in the mixture, are called nucleation sites (Clerc and Cleary, 1995; Schmelzer et al., 2004). Classical Nucleation Theory (CNT) describes phase separation in terms of a process involving the formation of a thermodynamically unfavorable phase separated 'nucleus' and an increasingly thermodynamically favorable process of 'growth'. In CNT, the processes of nucleation and growth involve the interplay between the cost of an interfacial surface energy, or surface tension, and a favorable volume energy resulting from molecular interactions in the segregated phase that permits the nucleus to grow by the addition of more material to the new phase. (A general description of the parameters involved in the classical nucleation theory is presented in the part B). However, in complex biological systems, such as the phase separation of lysozymes during crystallization, the CNT does not predict correctly the experimentally measured crystallization rates, which are ten orders of magnitude higher than the values predicted by CNT (Erdemir et al., 2009; Loh et al., 2017b; Vekilov, 2010). In these cases, non-classical nucleation models have been proposed, in which an additional step involving, for example, spinodal decomposition occurs before nucleation. For instance, a three-step mechanism has been proposed for the solidification and crystallization of gold nanocrystals based on liquid cell TEM studies (Loh et al., 2017a), which predicts that spinodal decomposition occurs before solidification and crystallization. Specifically, first, gold-rich spinodal structures form that later condense into amorphous nanoclusters, which crystallize into nuclei that can support nanoparticle growth because of their stable size (Ji et al., 2007; Loh et al., 2017b; Pong et al., 2007).

B. Principal equations of liquid phase transition

In a multicomponent system of two or more phases, the phase equilibrium criterion is that the chemical potential of a given component *i* must be equal in all phases where *i* is present:

$$\mu_i{}^\alpha = \mu_i{}^\beta = \mu_i{}^\gamma \ldots \text{ with } \mu_i = \left(\frac{\partial G}{\partial n_i}\right)_{T,P,n_{j \neq i}} \quad (1)$$

where μ_i represents the chemical potential of the *i*th component and α, β, γ, … represent the different phases where *i* is present at equilibrium (Clerc and Cleary, 1995). The compositions of those two phases α and β (expressed as the mole fraction of component B in these phases in figure S9B) are fixed at a given temperature but change as a function temperature. The collection of points defining the composition as a function of temperature at which these two phases coexist defines the binodal curve in the phase diagram (Figure S9B) (Alberti et al., 2019; Clerc and Cleary, 1995; Shin and Brangwynne, 2017).

Classical Nucleation Theory

Nucleation is the process by which a different thermodynamic phase with low free energy is formed from a parent phase with high free energy. The most common theoretical model to describe nucleation is the classical nucleation theory (CNT) that was formulated to explain the condensation of vapor into a liquid and that can be used also in liquid-solid equilibrium systems. In homogeneous nucleation, large supersaturations are usually needed to initiate the process because there are no preferential nucleation sites and the nuclei tend to form with equally low probability anywhere in the original mix (Karthika et al., 2016; Thanh et al., 2014).

For a spherical nucleus with radius *r*, the Gibbs free energy change $\Delta G(r)$ comprises the contributions of the volume free energy and the interfacial or surface energy cost of creating a nucleus inside the other phase (Equation 2; Figure S9C),

$$\Delta G(r) = \frac{4\pi}{3} r^3 \Delta G_v + 4\pi r^2 \gamma \quad (2)$$

where γ is the surface tension around the nucleus and ΔG_v is the free energy per unit volume gained from molecular interactions. The unfavorable interfacial energy dominates at small nucleus sizes r, while the favorable volumetric contribution to the nucleation barrier dominates at large nucleus sizes. The critical size or radius (r^*) for the nucleus corresponds to the minimum size beyond which the particle can be present in solution without being redissolved (Figure S9C). From equation (2), $r^* = -\frac{2\gamma}{\Delta G_v}$. As shown in figure S9C, ΔG^* indicates the nucleation barrier for the appearance of the separated phase. Clusters with values below r^* tend to redissolve and the ones with values above r^* tend to grow, thus, beyond r^*, $\Delta G(r)$ decreases with increasing r and at $r_0 = -\frac{3\gamma}{\Delta G_v}$, $\Delta G(r) = 0$. For $r > r_0$, $\Delta G(r)$ is negative and particle growth leads to the formation of a new phase. Thus, phase separation from these nuclei can proceed through a process of growth that takes place when the surface energy price of creating a discrete phase in the medium is overcome by the energy gained inside the nucleus by the addition of more material to the phase. Several authors have estimated, using experimental data and simulations, that the size of the critical nucleus is in the range of ~10-1,000 molecules. For instance, Yau and Vekilov reported that the size of the critical nucleus of protein apoferritin is about 40 nm in aqueous solution (Karthika et al., 2016; Yau and Vekilov, 2001).

Spinodal Decomposition and the Cahn-Hilliard Equation

To evaluate the thermodynamics and kinetics underlying spinodal decomposition, it is necessary to use a theoretical framework that incorporates fluctuations in the composition field $c(x,t)$. The Cahn-Hilliard (CH) model considers spatial inhomogeneities by adding a correction to the free energy function of a homogeneous medium. Based on the Ginzburg-Landau free energy theory (Cahn and Hilliard, 1958, 1959; Lee et al., 2014), the total free energy of a volume V of an isotropic system with a non-uniform composition is given by equation (3):

$$G[c(x,t)] = N_V \int [\bar{g}(c(x,t)) + \frac{1}{2}\kappa(\nabla c(x,t))^2]dV \quad (3)$$

where N_V is the number of molecules per unit volume, $\bar{g}(c(x,t))$ is the free energy per molecule of the homogenous system, $\nabla c(x,t)$ is the local composition gradient, and κ is a parameter that controls the free energy cost of variations in concentration. Thus, the free energy of a volume of a non-uniform solution can be expressed as the sum of the free energy that this volume would have in a homogenous solution, and a gradient energy that is a function of the local composition. In this theoretical framework, the chemical potential is redefined as the functional derivative of G (equation (3)):

$$\mu \equiv \frac{\delta G}{\delta c} = \bar{g}'(c(x,t)) - \kappa\nabla^2 c(x,t) \quad (4)$$

where $\bar{g}'$ is the first derivative of the free energy per molecule with respect to concentration. During phase separation, fluctuations in the concentration of components will lead to the increase of concentrations of certain components at the expense of depletions on other regions. Therefore, a flux of components will be produced. The flux of components in mixture (J) can be described by an alternative formulation of Fick's first law considering the variations in chemical potential (μ) (equation (5)):

$$J \equiv -M\nabla\mu \quad (5)$$

where M plays a role of the mobility (similar to the diffusion constant D used in Fick's first law) defined as an interface parameter that indicates a measure of the transport kinetics across the interface of the phases (Kim et al., 2016). Using a continuity equation (conservation of mass):

$$\frac{\partial c(x,t)}{\partial t} = -\nabla \cdot J \quad (6)$$

and by replacing equation (5) in the flux term (J), we obtain:

$$\frac{\partial c(x,t)}{\partial t} = M\nabla^2\mu \quad (7)$$

The replacement of equation (4) in equation (7) generates the Cahn-Hilliard equation, which describes the temporal evolution of the concentration field $c(x,t)$ during spinodal decomposition:

$$\frac{\partial c(x,t)}{\partial t} = \nabla \cdot [M\nabla\left(\bar{g}'(c(x,t)) - \kappa\nabla^2 c(x,t)\right)] \quad (8)$$

The CH equation is nonlinear and usually requires numerical approximations such as finite element, finite difference, or spectral methods to solve it. Spectral methods are common methods involving the use of fast Fourier transforms to solve differential equations. Computational simulations on the evolution of spinodal decomposition depicted by the CH equation are shown in figure S9D (Kim et al., 2016; Lee et al., 2014).

Some general implications can be obtained by evaluating particular conditions. For instance, for the double-well potential Gibbs free energy function (as the one depicted in figure S9A), the concentration profile on the interface between the phases is diffuse and has a sigmoidal shape. In particular, for the one-dimensional case, it has the form:

$$c(x) = tanh(\frac{x}{l})$$

with $l = \Delta c \sqrt{\frac{\kappa}{\Delta g}}$ representing the interfacial width, where $\Delta c = x_+ - x_-$, the width of the miscibility gap and where $\Delta g \geq kT$. By evaluating how the CH equations responds to small fluctuations in concentration of form $\delta c = A cos(kx - \omega t)$ where k is given by $2\pi/\lambda$ and where λ is the wavelength of the concentration perturbation (as in a Fourier series), it can be shown that the critical wavelength has the following expression:

$$\lambda_{max} = \frac{2\pi}{k_{max}} = 2\pi \sqrt{\frac{2\kappa}{-g''(c_0)}} \quad (9)$$

where g'' is the second derivative of the free energy with respect to concentration and the critical or maximum wavelength (λ_{max}) is the most unstable wavelength in which random fluctuations decompose into characteristic patterns (Figure S9D). There are two important conclusions from equation (9): i) λ_{max} only has a physical meaning when $g''(c_0)$<0 (a requirement for spinodal decomposition as discussed previously), and ii) λ_{max} gives a sense of the scale of the fluctuations and the size of domains formed during spinodal decomposition.

When one phase is at higher concentration, the Cahn–Hilliard equation predicts the process of Ostwald ripening, which is a thermodynamically-driven spontaneous process where the lower concentration phase forms spherical particles, and the smaller particles are absorbed through diffusion into the larger ones. The radii of these particles

grow in time as in $t^{1/3}$ (Lifshitz–Slyozov law) and the volume grows linearly with time. This process is favorable because the smaller particles are less energetically stable due to their high surface to volume ratio meaning high surface energy (Kim et al., 2016; Lee et al., 2014).
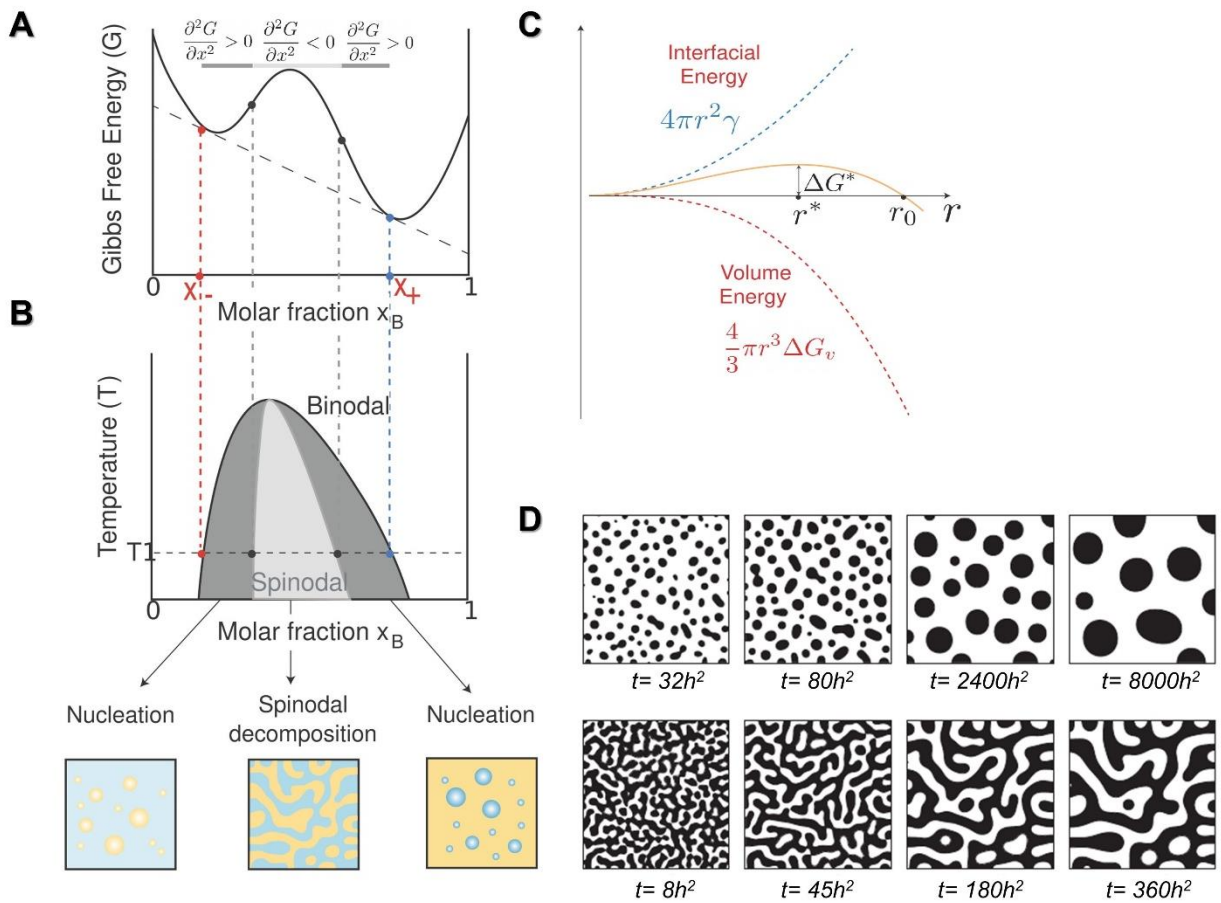
Figure S9. Schematics of phase transition mechanism, related to STAR Methods

(A) Gibbs' free energy as a function of molar fraction for a system that shows phase separation for a composition range $X_- < X_B < X_+$. The straight dashed line is the only common tangent. (B) The light gray color area is the instability region in which the system undergoes demixing through spinodal decomposition. In the area in between the binodal and spinodal, the system demixes via nucleation and growth (Alberti et al., 2019; Clerc and Cleary, 1995). (C) Gibbs free energy diagram for nucleation indicating the presence of a critical nucleus (r^*) and a nucleation barrier (ΔG^*) to overcome for growth to occur (Karthika et al., 2016). (D) Examples of spinodal decomposition predicted by the CH equation with different values of average composition and double-well potential function ($\bar{g}(\phi) = 0.25(\phi^2 - 1)^2$), where ϕ is the composition of the system. The timescale h is a parameter used in the simulation and has the value of spatial step (similar to the area splitted in a grid). For this particular simulation, h= 0.03 (Image was taken from (Kim et al., 2016)).